TECHNISCHE UNIVERSITÄT WIEN
Vienna University of Technology

DIPLOMARBEIT

Collective modes in $BaNi_2As_2$

Zur Erlangung des akademischen Grades

Diplom-Ingenieur

im Rahmen des Studiums

Technische Physik

Eingereicht von

Arjan Mejaš
Matrikelnummer 01328234

Ausgeführt am Institut für Festkörperphysik
der Fakultät für Physik der Technischen Universität Wien

Betreuung
Betreuer: Prof. Dr. Neven BARIŠIĆ

Wien, 23.08.2021

(Unterschrift Verfasser) (Unterschrift Betreuer)

Abstract

$BaNi_2As_2$ is metallic compound, susceptible to density-wave formation. Previous studies on $BaNi_2As_2$ have revealed the existence of two types of periodic lattice distortion above and below the tetragonal to triclinic structural phase transition (T = 137 K), suggesting Charge-density-wave (CDW) order to compete with superconductivity. In order to study the density-wave formation and determine its origin, we have applied within the framework of this thesis, several experimental methods on high-quality $BaNi_2As_2$ single crystals.

First, Laue diffraction was used to determine the crystal structure and to orient the $BaNi_2As_2$ single crystals. Next, transport measurements of resistivity were undertaken to carefully characterize the samples and investigate the compound's behaviour at low temperatures, while being exposed to external magnetic field. Those measurements have confirmed the presence of the phase transition (from tetragonal to triclinic phase) at around 137 K upon cooling. Finally, on highest quality samples, time-resolved femtosecond optical spectroscopy was applied. Aim was to reveal the existence of collective CDW amplitude modes and to study their origin. The evolution of these modes through the structural phase transition implies the CDW order in the triclinic phase smoothly evolves from the unidirectional CDW in the tetragonal phase and suggests that the CDW order drives the structural phase transition.

Acknowledgements

I would in particularly like to thank Dr. Tao Dong who had greatly supported the pump-probe optical spectroscopy measurements by numerous discussions, shared ideas and visions, as well as Vladimir Grigorev, who has been a great help at the experimental part of my work. I would also like to thank Prof. Dr. Jure Demšar for the given opportunity to work on this experiment as a part of his group at the Johannes-Guttenberg University and for his help with arranging my stay in Mainz.

I must not forget to thank Dr. Wojchiech Tabiś who has been a great help at the execution of X-ray, magnetometry and transport measurements at TU Wien and has supported me at their theoretical evaluation and data analysis with his advice and guidance. I would like to thank as well as Benjamin Klebel, who has been a great help at the experimental part of my work at TU Wien.

Special thanks also go to Dr. Amir-Abbas Haghighirad from Karslruhe Institute of Technology, for his work on the synthesis of $BaNi_2As_2$ samples as well as Prof. Dr. Matthieu Le Tacon for sharing their samples with us.

Finally, I warmly thank my principal advisor Prof. Dr. Neven Barišić at TU Wien for his mentorship and guidance, not only during working on this thesis, but also during the last eight years of our acquaintance, whose wisdom has profoundly shaped me and with no doubt influenced me to become the person I am today.

Contents

Chapter 1

1. Introduction

Over the past fifty years, the ability to grow a wide range of crystalline materials and numerous experimental improvements have enabled the research of fundamental physical principles in well-defined and well-controlled environments with unprecedent precision. One intriguing avenue of research has been focused on the effects of reduced dimensionality of an electron gas, experiencing an external periodic potential. These effects have been explored through investigations of quasi-one (Q-1D) and quasi-two-dimensional (Q-2D) metallic materials and have been additionally advanced by several important theoretical predictions.

Amongst the most important theoretical advances in this field were the predictions made by Peierls [1], Fröhlich [2] and Kohn [3]. Peierls asserted that a metallic one-dimensional atomic chain would be susceptible to a periodic lattice-distortion creating a modulation in the electron-density along the chain known as the charge-density-wave (CDW) order [1]. Around the same time, Fröhlich established that the density-wave is a coherent superposition of electron-hole pairs, and he furthermore outlined the changes in a crystal‘s band structure due to the formation of a density-wave [2]. Kohn contributed to the field by outlining the effects a density-wave would have on the lattice dynamics in a one-dimensional system. Importantly, this work highlighted the susceptibility of metallic systems with large electronic anisotropies to a phase where either the charge or spin density is modulated along the crystal lattice [3].

The breakthrough came with the synthesis of inorganic quasi-one and quasi-two-dimensional materials which allowed controlled investigations of electronic correlations in these materials. Experimental research has revealed much. Perhaps the most famous discovery is the high temperature superconductivity in the cuprates [4]. This research has also led to the confirmation of theoretically predicted phases such as the spin-density-wave and charge-density-wave states.

Much of the current work in this field has focused on the relationship between the density-wave states and the superconductivity observed in some of these materials [5].

Hence, the aim of this thesis is to contribute to the understanding of the CDW order in a Q-2D metallic material. The CDW is an important concept in condensed matter physics, germane to several macroscopic quantum phenomena such as high-temperature superconductivity, colossal magnetoresistance, ferrimagnetism and ferromagnetism, which arise from a delicate balance between different interactions among electrons, phonons and spins [6]. The study of the interplay among these various degrees of freedom in strongly coupled electron-lattice systems is thus crucial to their understanding and for optimizing their properties. Finally, CDW materials with their inherent modulation of electron density and the associated periodic lattice distortion, represent the ideal set of systems for the study of highly cooperative phenomena [7].

One such material is Barium Nickel Arsenide, further referred to as $BaNi_2As_2$. It is a Q2-D non-magnetic analogue of $BaFe_2As_2$, the parent compound of the archetype ferropnictide high-temperature superconductor [8]. Recent diffraction studies on $BaNi_2As_2$ demonstrated the existence of two types of periodic lattice distortions: one above and one below the tetragonal to triclinic phase transition ($T = 137$ K) upon warming, suggesting a potential CDW order phase transition [9]. CDW materials, such as $BaNi_2As_2$, with their inherent modulation of the electron density and associated periodic lattice distortion, represent ideal model systems for a careful study of such highly cooperative phenomena [10].

Within the framework of this thesis, the time-resolved femtosecond optical spectroscopy has been applied to demonstrate the existence of collective CDW amplitude modes, uncover their origin, and understand their evolution in single crystals of $BaNi_2As_2$. Ultrafast spectroscopy allows to study the carrier dynamics and coupling strengths between electrons and other degrees of freedom in solids. In general, numerous materials are investigated with time-resolved spectroscopy, ranging from well understood systems, such as metals and semiconductors, to advanced materials with complex low temperature orders, like high-temperature superconductors and ferromagnets [11].

Chapter 2

2. Charge density waves

2.1 Brief overview

The CDW order is a periodic modulation of the charge-carrier density. It is a Fermi-surface-driven phenomenon, frequently accompanied by the lattice instability and a periodic lattice distortion (PLD). Below the transition, the electron subsystem opens a gap, lowering the energy for the occupied states. Due to electron-phonon interaction, this energy gain is greater than the energy loss due to lattice deformation [20].

The concept of the CDW permeates much of the condensed matter physics and chemistry, and have their origin rooted in the instability of a one-dimensional (1D) system described by Peierls [1]. The extension of this concept to higher dimensional problems has led to the concept of Fermi surface nesting (FSN), which defines the wave vector ($\mathbf{q}_{CDW}$) of the CDW and the corresponding lattice distortion. The principal idea is that the $\mathbf{q}_{CDW}$ connects segments of the Fermi contours, resulting in the effective screening for phonons. The latter induces the Kohn anomaly in the phonon dispersion near $\mathbf{q}_{CDW}$ [3], with a dramatical softening of phonon modes. Consequently, this drives the phase transition and a change of the lattice symmetry below the transition temperature, T_{CDW} [24]. While CDWs also occur in materials with two- or three-dimensional band structures, they are predominantly a one-dimensional phenomenon [25], since the reduced dimensionality of the system enhances divergent behaviours.

In Chapter 2, the concepts fundamental to the understanding of CDW will be presented; the key aspects of Peierls' model, which include the Fermi surface nesting in the electronic structure, a sharp peak in Lindhard function, the Kohn anomaly in phonon spectra, a structural transition in a crystal lattice, and the metal to insulator transition.

2.2 The effect of lattice distortion

Let us consider a special case of 1D metal with lattice constant a at the temperature of 0 K. We assume that the system consists of N periodically arranged atoms, forming a linear chain along the x direction. Consequently, the size of the system is $L = Na$ [19].

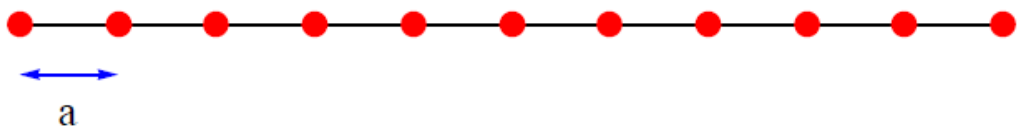

Figure 2.1: 1D chain of atoms with nearest neighbour distance (NND) of a [18].

Due to periodicity of the lattice potential in which electrons move, the energy gap in the single-electron spectrum appears at the Brillouin zone boundary ($k = \pm\frac{\pi}{a}$), being fixed at this reciprocal lattice points. As well known, there are $2N$ states in the first Brillouin zone ($|k| \leq \frac{\pi}{a}$)[19]. The factor *2* amounts for the two possible spin configurations of the electrons.

When there are $2N$ electrons in the system, the band is filled up to the Brillouin zone. Consequently, at such a filling material is an insulator or semiconductor, depending on how large the gaps between fully occupied and empty bands are. On the other hand, when, for example, each of the atoms involve one electron in the band, the band is half-filled – and the material should behave as a metal [19].

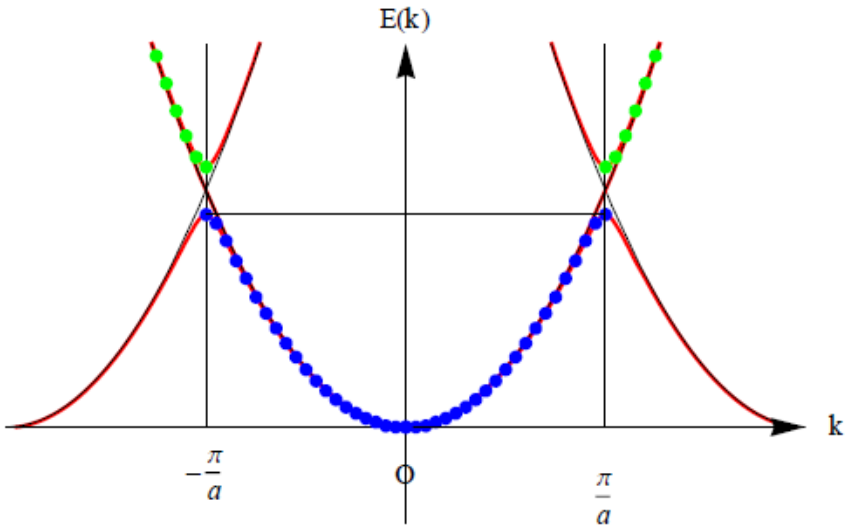

Figure 2.2: Energy band for the system with two electrons per atom. All states are occupied up to the Brillouin zone (insulator) [18].

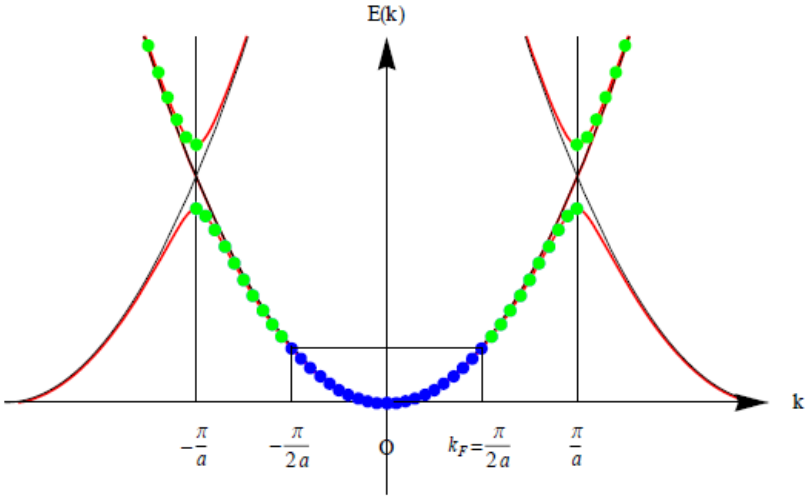

Figure 2.3: Energy band for the system with one electron per atom. All states are occupied for $|k|<k_F=\frac{\pi}{2a}$ (k_F = Fermi wave number) inside of the Brillouin zone (metal) [18].

However, if the lattice is subjected to an external force and distorted with a period of $\lambda = k_F = \frac{\pi}{2a}$, the atomic displacements act as a new periodic potential. This involves a new Brillouin zone at $\pm k_F$ and opens an energy gap at $k = k_F = \pm\frac{\pi}{2a}$ in the dispersion relation $E(k)$ [19].

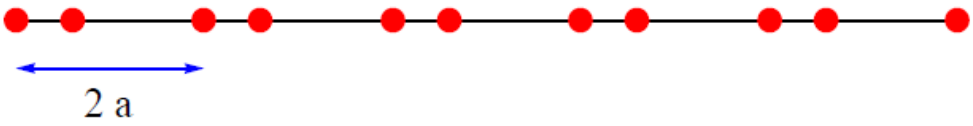

Figure 2.4: Change of NND from a to $2a$ due the lattice distortion [18].

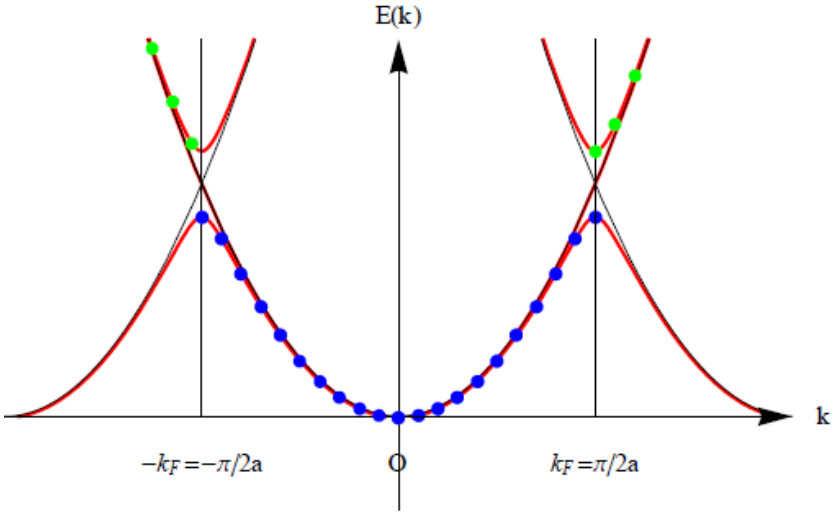

.Figure 2.5: Energy band after the lattice distortion for the system with one electron per atom. The energy gap opens now at $k = k_F = \frac{\pi}{2a}$ [18].

2.3 The Peierls transition

In his attempt to explain the electronic properties of bismuth, Peierls pointed out that 1D metals are unstable at low temperatures [21]. An opening of a bandgap at the Fermi energy E_F at k_F, which lowers the electronic energy of the crystal, accompanies the lattice distortion with the periodicity of $\frac{\pi}{2k_F}$. In other words, a new Brillouin zone at $\pm k_F$, is formed in response to the new crystal structure. All the states, which are raised by this change, are empty, whereas all the states, which are lowered by this change, are occupied. In a perfect 1D metallic crystal these changes result in a completely gapped Fermi-surface and a metal to insulator transition at T_C [21]. For 1D systems, the energy cost of distortion is always lower than gain in the electronic energy, which makes 1D materials inherently unstable to the transition in the case of commensurable new structures [20].

Figure 2.6(a) illustrates an atomic model of such a 1D chain with one electron per atomic site above T_C, while Figure 2.6(c) shows the corresponding free electron band structure. In this 1D case, the only zero energy transition between electrons is from k_F to $-k_F$ (or vice versa).

In the half-filled cases, the Fermi points are at $k_F = \pm\frac{\pi}{2a}$ and are connected by a wave vector $q = 2k_F$. Figure 2.6(b) illustrates an atomic model of such restructured chain below T_C while Figure 2.6(d) shows the corresponding electronic band structure in the new zone [25].

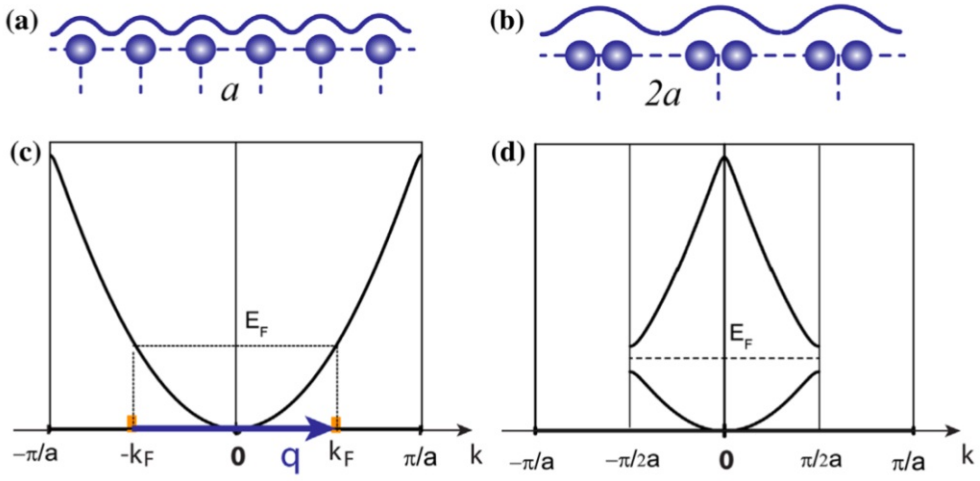

Figure 2.6: Chain of atoms with respective energy band gaps before (a) and after (b) a PLD in a hypothetical 1D metal. (c) and (d) illustrate the band structure for the chains presented in (a) and (b), respectively [25].

Temperature dependence

In a metal, the electron density is highly uniform, and the equilibrium positions of the ions usually form a perfectly periodic lattice. Due to Peierls physics, when temperature is lowered, the Fermi surface of a metal may become unstable below a transition's critical temperature T_C.

Depending on the system and types of interaction, this Fermi surface instability leads to redistributions of the charge carrier density and forms a periodic spatial modulation. This modulation of the electron density is called a charge density wave (shorter CDW), a phrase first discussed by Fröhlich in 1950's. By coupling to the lattice, it changes the ion potential in the lattice so that the ions move to new equilibrium positions. Static CDW is always accompanied with a periodic lattice distortion [25].

2.4 Kohn anomaly & Fermi surface nesting

In 1959, Walter Kohn pointed out that lowering the energy of the system and a reconstruction of the crystal lattice, result in a simultaneous softening of phonons (vibrational modes of the lattice) [24]. Consequence of phonon softening is the renormalization of the phonon mode $\chi_0(q)$, with a wave number close to $2k_F$, referred to as the Kohn anomaly [28]. Namely, this renormalization causes a suppression of the effective elastic constant and the energy of the phonon decreases. The origin of the renormalization is the interaction with the electron subsystem.

The phonon renormalization is strongly temperature-dependent, with the phonon energy decreasing to zero when the temperature approaches T_c. This frozen phonon at T_c leads to a second-order phase transition into the CDW state [25]. Above the temperature of the transition, the thermal fluctuations too strong for this static deformation set in.

Fig. 2.7 shows the ideal phonon dispersion for this 1D chain at different temperatures. In theoretical modelling, below T_{CDW}, the phonon energy at $q = 2k_F$ becomes imaginary, meaning there is a new lattice structure. Above T_{CDW}, there is a sharp dip (Kohn anomaly) in the phonon dispersion but no static reconstruction [24].

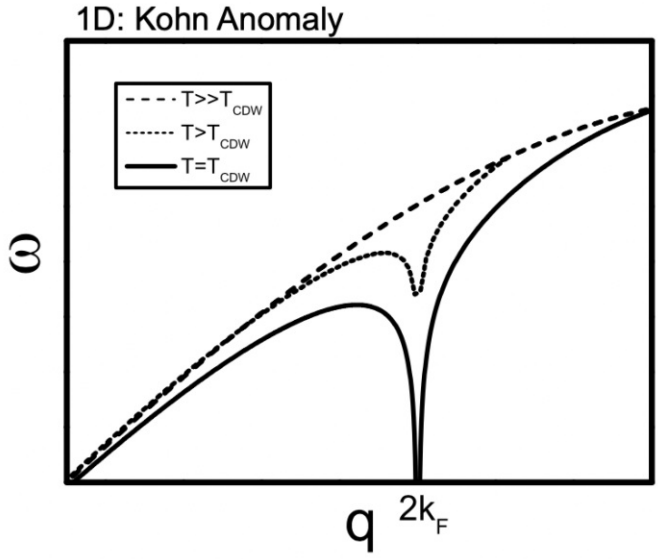

Figure 2.7: Kohn anomaly in the acoustic phonon branch as a function of temperature [24].

The extension of this concept to the systems with reduced dimensionality has led to the concept of Fermi surface nesting (FSN), which determines the wave vector ($\mathbf{q}_{CDW}$) of the CDW and the corresponding lattice distortion [24]. The Fermi surface nesting occurs when there are two parallel parts of the Fermi surface, such that a single q-vector can connect many points on these two parts, as presented schematically in Fig. 2.8. The "ideal" 1D metals have perfect nesting conditions since the Fermi surface consists of two planes at $k = \pm k_F$. In higher dimensions, for a free-electron-like single-band metal with nearly circular or spherical Fermi surface no nesting is expected to occur. However, the nesting is still possible in systems with stronger interactions or quasi 1D bands [23].

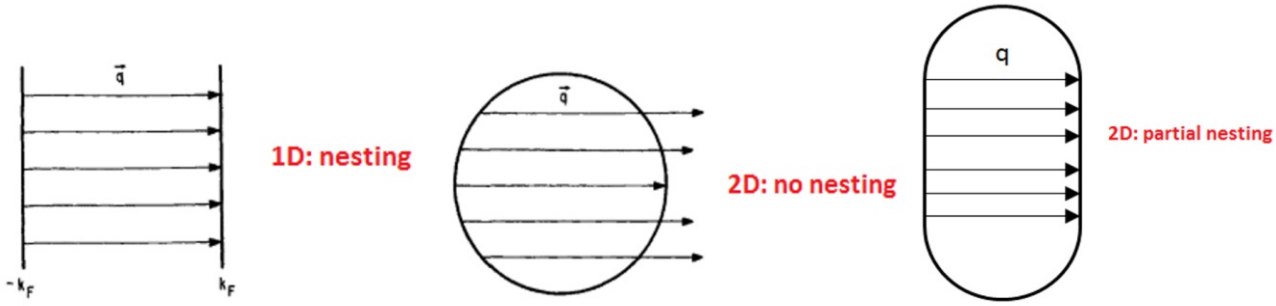

Figure 2.8: Fermi surface nesting in system with different effective dimensionality [22].

2.5 Mean field theory of Peierls

To describe the Peierls transition one must consider the interaction between electrons and the lattice. Neglecting the electron-electron interactions the electron-lattice system can be described by the *Fröhlich Hamiltonian H* [21], given by

$$H = H_{el} + H_{ph} + H_{el-ph}. \qquad (2.1)$$

where H_{el} is the Hamiltonian of the electron system, H_{ph} the Hamiltonian of the lattice vibrations and H_{el-ph} the Hamiltonian of interaction between the electron and phonon system. The Hamiltonian describing the electron subsystem involves free electrons and it is given by [21]

$$H_{el} = \sum_k \epsilon_k a_k^\dagger a_k \tag{2.2}$$

where a_k^+ and a_k are electron creation and annihilation operators, respectively, and $\varepsilon_k = 2\hbar^2k^2/2m$ is the electron dispersion in the long-wave limit. Electrons are regarded as spinless, as it is taken that spin degrees of freedom do not affect the transition. The part of the Hamiltonian that describes the collective motions of the lattice ions H_{ph} is given by [21]

$$H_{ph} = \sum_q \frac{P_q P_{-q}}{2M} + \frac{M\omega_q^2}{2} Q_q Q_{-q} \tag{2.3}$$

where P_q is the momentum of a vibrating ions, M is the mass of an individual ion, Q_q are normal phonon coordinates and ω_q are frequencies of the normal modes. Rewritten in the Hamiltonian in the formalism of second quantization, the phonon part of the Hamiltonian reads [21]

$$H_{ph} = \sum_q \hbar\omega_q (b_q^\dagger b_q + 1/2) \tag{2.4}$$

where b_q^+ and b_q are creation and annihilation operators for phonon excitations, characterised by wave vector q.

For interaction between phonons and electrons it is assumed that the ionic potential at any point depends only on the distance from the centre of the atom. Marking the equilibrium lattice positions as R and the displacements with u, in the formalism of the second quantization, this interaction part of the Hamiltonian may be expressed as follows [21]

$$\begin{aligned} H_{el-ph} &= \sum_{k,k',R} \langle k| V(r-R-u) |k'\rangle a_k^\dagger a_{k'} \\ &= \sum_{k,k',R} e^{i(k'-k)(R+u)} V_{k-k'} a_k^\dagger a_{k'} \end{aligned} \tag{2.5}$$

where $V_{k\text{-}k'}$ is Fourier component of atomic potential $V(r)$ and $|k\rangle = 1/\sqrt{L}\, e^{ikr}$. If the displacements are small, the exponential term can be expanded as

$$
\begin{aligned}
e^{i(k'-k)u} &\approx 1 + iu(k'-k) \\
&= 1 + \frac{i}{\sqrt{N}}(k'-k)\sum_q u_q e^{iqR}
\end{aligned}
\tag{2.6}
$$

where the displacement of ion is given in terms of Fourier transforms. Clearly, the interaction Hamiltonian has two parts. The first part includes the equilibrium ion positions and it is responsible for the transformation of free electron spectrum into the band structure. The interaction term that describes phonons, i.e., vibrations around equilibrium positions, may be rewritten as [21]

$$
\begin{aligned}
H_{el-ph} &= \frac{i}{\sqrt{N}} \sum_{k,k',R,q} e^{i(k'-k+q)R}(k'-k)u_q V_{k-k'} a_k^\dagger a_{k'} \\
&= i\sqrt{N}\sum_{k,k'}(k'-k)u_{k-k'}V_{k-k'}a_k^\dagger a_{k'} \\
&= \sum_{k,q} g_q(b_{-q}^\dagger + b_q)a_{k+q}^\dagger a_k,
\end{aligned}
\tag{2.7}
$$

where the electron-phonon coupling constant is

$$
g_q = i\left(\frac{\hbar}{2M\omega_q}\right)^{1/2}|q|V_q \tag{2.8}
$$

Now, by collecting all the terms, one can construct the Fröhlich Hamiltonian [21]

$$
H = \sum_k \epsilon_k a_k^\dagger a_k + \sum_q \hbar\omega_q b_q^\dagger b_q + \sum_{k,q} g_q(b_{-q}^\dagger + b_q)a_{k+q}^\dagger a_k \tag{2.9}
$$

If a transition to a distorted state occurs, the lattice will be distorted. This distortion correspond to the static, non-zero expectation value of $\langle b_q \rangle = \langle b_q^+ \rangle$. It is not obvious which value of q will lead to a transition. From linear response theory for 1D gas, one can predict that the critical value is $q = 2k_F$. In particular, we can define a complex order parameter below the transition as [21]

$$
\Delta e^{i\phi} = g_{2k_F}\langle b_{2k_F} + b_{-2k_f}^\dagger \rangle \tag{2.10}
$$

where Δ and ϕ are both real. The displacement of atoms, corresponding to the static deformation, is then given by [21]

$$\langle b_{2k_F} + b^{\dagger}_{-2k_f}\rangle e^{i2k_F x} + c.c = \frac{2\Delta}{g_{2k_F}} cos(2k_F x + \phi) \tag{2.11}$$

In the ordered phase, the electron part of the Hamiltonian can be diagonalized by substituting phonon operators with their expected values and using linear dispersion relation for behaviour of electron band near ε_F. Finally, using order parameter as defined in Eq. 2.10, *Fröhlich Hamiltonian H* in the presence of the static lattice distortion may be rewritten as [21]

$$\begin{aligned} H &= \sum_k \epsilon_k a^{\dagger}_k a_k + 2g \sum_k [a^{\dagger}_{k+2k_F} a_k \langle b^{\dagger}_{-2k_F}\rangle + a^{\dagger}_{k-2k_F} a_k \langle b_{-2k_F}\rangle] + 2\hbar\omega_{2k_F} \langle b_{2k_F}\rangle^2 \\ &= \sum_k \left[\epsilon_k a^{\dagger}_k a_k + |\Delta| e^{i\phi} a^{\dagger}_{k+2k_F} a_k + |\Delta| e^{-i\phi} a^{\dagger}_{k-2k_F} a_k\right] + 2\hbar\omega_{2k_F} \langle b_{2k_F}\rangle^2 \end{aligned} \tag{2.12}$$

2.6 Lindhard response function

To desribe the formation of the CDW, a model of free electron gas is often employed. The response of an electron gas to an external perturbation is described by the Lindhard response function $\chi_0(q)$. This response is closely related to the excitation of the electron system. In 1D, the real part of $\chi_0(q)$ has a divergent behaviour, characterized by the singularity at $q = 2k_F$, as shown in Fig. 2.9. Since the lattice polarization is proportional to the electron response function, which means the 1D electron gas coupled to the lattice is unstable [25].

The basic idea of CDW in two- or three-dimensions is that CDWs can occur in systems with Fermi surface nesting since the electronic system looks Q-1D along the direction where nesting occurs. A more complex treatment involves calculation of the Lindhard response function with a particular Q-1D electron dispersion, which describes the rearrangement of charge density in response to a perturbation. That is, the zero-energy (static) value of the Lindhard response function $\chi_0(q)$ is used to determine whether the electron response can drive a CDW phase transition. If so, there should be a syngularity in the imaginary part of the response function Im[$\chi_0(q)$] at the Fermi surface nesting vector as well as in the real part Re[$\chi_0(q)$] since the real part defines the stability of the system. This is a common way of demonstrating that CDWs are more certain to occur in 1D,

but less energetically favourable in 2D or 3D systems, unless the Fermi surface has a stronger 1D character [24].

An electronic system with density given by $\varrho(r)$, when subjected to an external potential $\psi(r)$, will experience a redistribution of its electrons creating a change in the electron density. The distribution of the electrons

$$\rho(r) = \psi(r)\chi(r) \tag{2.13}$$

is dependent on the external potential and the coupling of this potential to the electron gas $\chi(r)$. The response function in the static limit can be described by the *Lindhard function* of the form

$$\chi(\mathbf{q}) = \int \frac{d\mathbf{k}}{(2\pi)^d} \frac{f_k - f_{k+q}}{\epsilon_k - \epsilon_{k+q}} \tag{2.14}$$

where f_k is the *Fermi-Dirac distribution* and ε is the dispersion relation for the electron gas. Both k and q are wave-vectors. In 1D system, this function diverges when the following condition is satisfied

$$\epsilon_k - \mu = \epsilon_{k+q} - \mu \tag{2.15}$$

where μ is the chemical potential. Due to differences between 3D and 1D systems, the Lindhard response is drastically different for these cases. The changes in the Lindhard function are made clear when it is displayed graphically at $T = 0$ [19].

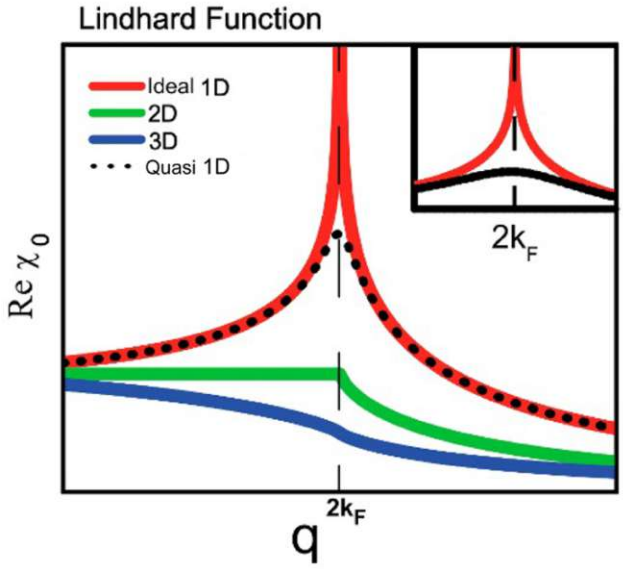

Figure 2.9: The Lindhard response function of ideal 1D, 2D (circle) and 3D (sphere) gas. [24]

In the 1D case the Lindhard function diverges at a wave vector $q = 2k_F$, whereas the 3D function only the first derivative is divergent. This can be explained by considering the topology of the respective Fermi-surfaces in 1D and 2D, as shown in Fig. 2.7.

The CDW ground state develops in low dimensional metals because of the electron-phonon interaction. It is characterized by a 2Δ gap in the single-particle excitation spectrum and by a collective mode formed by electron-hole pairs involving the wave vector $q = 2kF$. The atomic position of a linear chain associated with the collective mode is modulated as

$$\varrho(x) = \varrho_0 + \varrho_1 \cos(2k_F x + \phi) \tag{2.16}$$

where δ_0 is the electron density in the absence of modulation - above T_{CDW}, δ_1 is the magnitude of the density-wave, $2k_f$ is the wave-vector of the modulation and ϕ describes the phase of the modulation [19].

An energy gap opening at E_F near the Fermi level. The amplitude of this gap is given by

$$\begin{aligned} \Delta &= 2\epsilon_F e^{-1/\lambda} \\ \lambda &= \frac{g_{2k_F}^2}{\hbar\omega_{2k_F}} \end{aligned} \tag{2.17}$$

where λ is dimensionless electron-phonon coupling constant. As seen in Fig. 2.8, the electron dispersion relation changes if a periodic potential is introduced [19]. The divergence of the Lindhard function results in a sinusoidal modulated solution of the Eq. 2.13, defining the modulation of the electron density at $T = 0$ as well,

$$\begin{aligned} \rho(x) &= \rho_0 + \frac{\Delta\rho_0}{\lambda v_F k_F} cos(2k_F x + \phi) \\ &= \rho_0 + \rho_1 cos(2k_F x + \phi) \end{aligned} \tag{2.18}$$

In addition to being dependent on q, the Lindhard response function is, due to the presence of the Fermi function in Eq. 2.14, also dependent on temperature.

When the nesting condition is satisfied ($q = 2k_F$) the temperature dependence takes the form

$$\chi(2\mathbf{k}_f, T) \propto \ln \frac{1.14\epsilon_0}{k_B T} \tag{2.19}$$

where ε_0 can be approximated to the Fermi-energy and k_B is the Boltzmann constant. This introduces the concept of a transition temperature T_{CDW} for which the value of $\chi(q,T)$ becomes large enough to result in a periodic solution to Eq. 2.18 [19].

2.7 Classification of the charge density waves

2.7.1 Types of orderings

As expected, the origin of charge density waves is strongly related to the dimensionality. There are at least three types of CDWs [25]. Type I CDWs are quasi-1D systems with their origin in the Peierls' instability, where the lattice distortion is a consequence of the lowering of electronic energy. The best example may be linear chain compounds [25]. Type II CDWs are driven by the electron phonon coupling but not by the Fermi surface nesting. Here the electronic and lattice instabilities are intimately tied to each other, and there is a phonon mode at $\mathbf{q}_{CDW}$, decreasing to zero at the transition temperature T_{CDW}. Formation of this type of CDW does not drive metal to insulator transition. Typical example of type II is quasi-2D layered material $NbSe_2$ [25]. Type III CDWs are systems with the charge modulation without indication of the Fermi surface nesting or electron-phonon coupling as the driving force. The best example of type III CDWs may be the cuprates which exhibit charge ordering phenomena. The electronic correlations are expected to play a significant role in the type III systems [25].

2.7.2 Coupling of electrons to the crystal lattice

CDW ground state can be also distinguished in respect to the coupling to the underlying lattice in three different types: commensurate, incommensurate and discommensurate.

The commensurate state is usually referred to as a "locked-in" state, where the periodicity of crystal lattice and CDW can be expressed by an integer number, such as a 2-fold or 3-fold supercell [29]. That is, CDW is commensurate, only if the wave vector describing the CDW is a rational number times one of the vectors which forms the reciprocal lattice crystal. In practice, the denominator of that rational number is small and independent of temperature [20].

If the ratio of lattice periodictiy and CDW periodicity is an irational number then the CDW is incommensurate, meaning that periodictiy of CDW can not be matched with the lattice. The incommensurate CDW state may not actually correspond to the lowest possible energy state. Hence the CDW may undergo a further distortion that makes it "twice commensurate". Here, the CDW wavevector is an integral fraction of the underlying lattice. Therefore, there can be two phase changes associated with a CDW formation: the normal-to-incommensurate transition (usually second order) and the incommensurate-to-commensurate transition (first order) [20].

Besides the states mentioned above, in the 1976 McMillan [30] introduced the concept of discommensurations, which are narrow out-of-phase regions between large in-phase (commensurate) regions. In this concept, the incommensurate-to-commensurate transition is viewed as a defect "melting" transition or discommensuration. In this state the supercell is composed of commensurate domains separated by phase slips of small incommensurate sections [29].
The coupling of electrons to the lattice can therefore be either commensurate (Fig. 2.10(A)), incommensurate (Fig. 2.10(B)), or discommensurate (Fig. 2.10(C)) - all of which lead to the formation of a supercell, where the atoms are displaced from their ideal positions in the crystal structure. Observing these modulations allows the crystallographic characterization of CDWs [29].

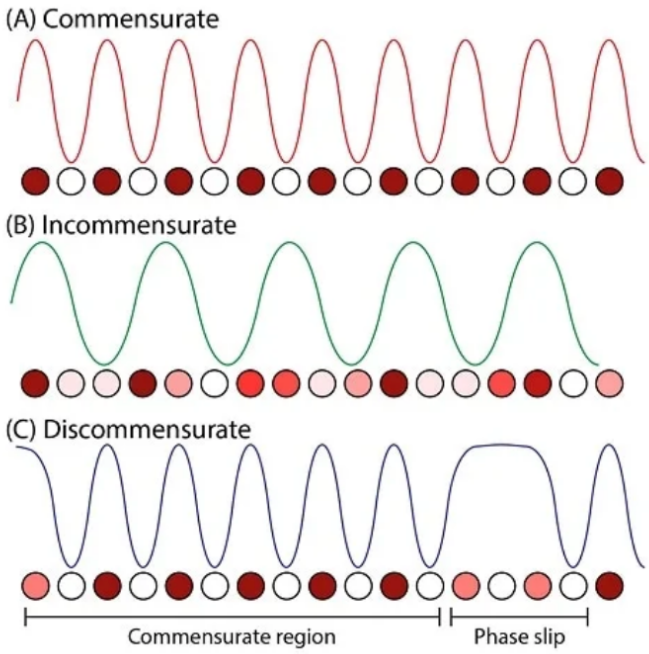

Figure 2.10. Illustration of a CDW in a (a) commensurate, (b) Incommensurate and (c) Discommensurate supercell [29].

2.8 Materials exhibiting charge density waves

2.8.1 CDW in Q-1D materials

A prime example of quasi-1D materials are molybdenum oxides $A_{0.3}MoO_3$ (called blue bronzes due to their shiny blue appearance), where A is a monovalent metal such as K, Rb, or Tl. They are well known for their interesting electronic properties arising from the 1D chain structures. Due to availability of large single crystals, blue bronze is the most intensively studied quasi-1D CDW material [31].

The first blue bronze in which CDW transition was found is $K_{0.3}MoO_3$, which crystallizes in a monoclinic unit cell at room temperature [32]. These materials also form long chains, composed of clusters of MoO_6 octahedra, separated with alkali ions. Common property of these compounds is their high (structural and) electronic band anisotropy.

There is strong overlap of *d* orbitals along the chain direction, while the chains are separated by K (and thus no considerable overlap) in perpendicular direction. This structure yields a highly anisotropic electronic response. Resistivity is smallest along the chain-direction whilst along the d-direction it is an order(s) of magnitude larger. Crystal structure of $K_{0.3}MoO_3$ is shown in Fig. 2.11 [32].

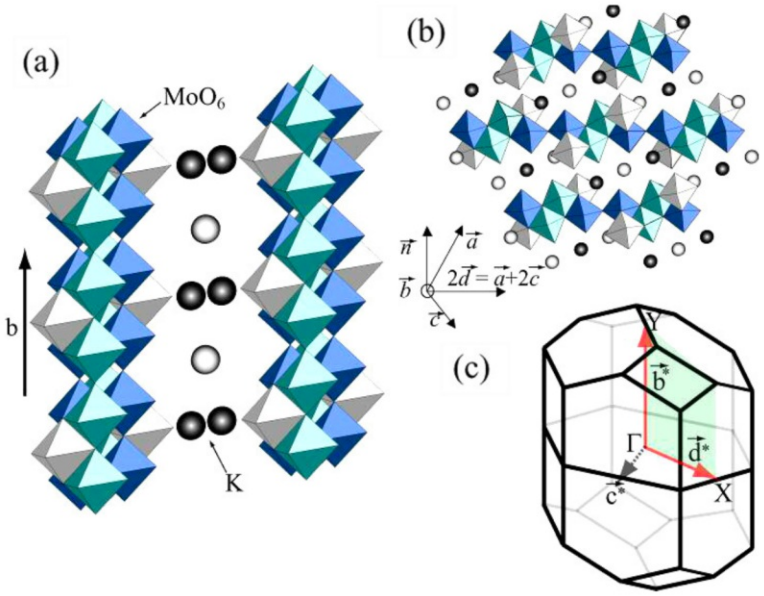

Figure 2.11: (a) Crystal structure of $K_{0.3}MoO_3$ at room temperature. (b) Cross section of the infinite chains with the *a*–*c* plane. (c) The Brillouin zone of $K_{0.3}MoO_3$ for the simple monoclinic structure [32].

These Q-1D crystals offer a well-defined system to explore the density-wave phase as well as to study its interaction with other phases, e.g., superconductivity. Based on research on this and similar compounds, qualitative features of the CDW phase such as the periodic-lattice-distortion, the electronic band-gap, band-backfolding, metal-to-insulator transition, and anomalies in heat-capacity measurements have been well documented for quasi-1D systems.

2.8.2 CDW in Q-2D materials

Layered compounds can often be considered as Q-2D and thus the theoretical approach differs from the 1D model. Nesting is often imperfect, and the Fermi-surface is only partially gapped in the CDW phase. Therefore, the density-wave transitions in these materials are in general less likely than in the Q-1D case.

Generally, it requires a strong electron phonon coupling to overcome the reduction in $\chi(q,T)$ caused by imperfect nesting at the Fermi surface. The transition-metal dichalcogenides are often used as an example of 2D CDW materials. These materials consist of chalcogen-metal-chalcogen layers bound together by weak van der Waals forces [34].

One extensively studied and instructive example of the dichalcogenides is 1T-TaS_2 [5]. In addition to several CDW phases which are driven by electron-phonon interactions, it enters a Mott-insulator state, governed by electron-electron interactions (see Fig. 2.12). In a wider context 1T-TaS_2 highlights, that electronically anisotropic materials which are susceptible to electronic instabilities can be used to study fundamental physical interactions [5].

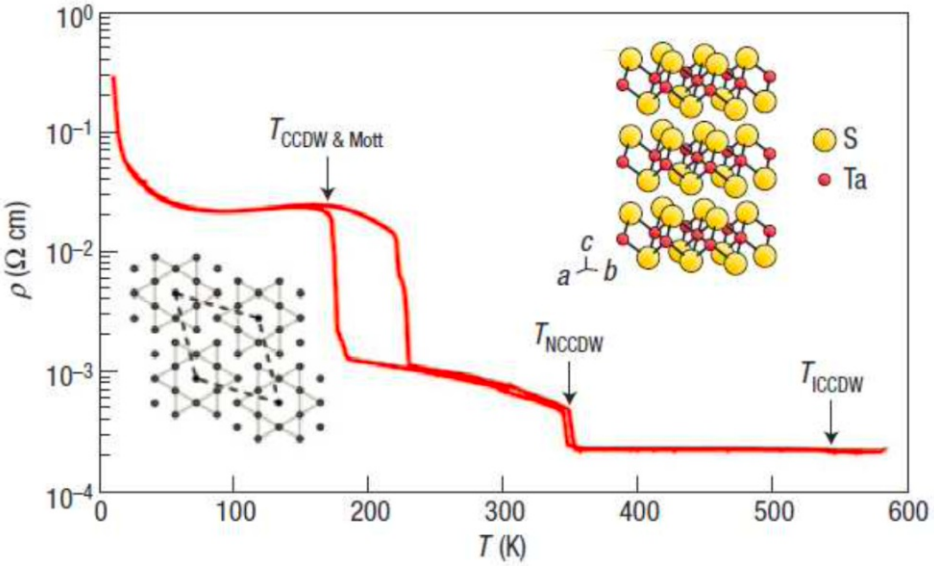

Figure 2.12: Temperature dependence of resistivity in 1T-TaS2 reveals a series of subsequent phases. The high-temperature incommensurate-CDW phase (ICCDW), the nearly-commensurate-CDW phase (NCCDW) and the commensurate-CDW phase are indicated. In the ICCDW phase, 1T-TaS2 is a metal and with the onset of the CCDW state it behaves as a Mott-insulator [5].

2.9 Instructive experimental methods and results

The formation of charge-density-waves within crystals leads to a number of experimentally observable effects. A number of experimental techniques can be used to characterize the material properties associated with a CDW. Here, some of them will be briefly discussed to provide a general overview of the experimental field [25].

2.9.1 Structure - real space

The direct measurement of the spatial charge modulation can be performed by scanning tunnelling microscopy (STM). The current flowing through the tip of the STM is proportional to density of states at a set bias voltage, thus enabling to direct visualisation of the waves [35]. The collected data can be used to determine the nesting vector, the wavelength of the charge modulation as well as the electronic transition temperature [43]. It also allows to simultaneously establish the energy-gap associated with the CDW formation.

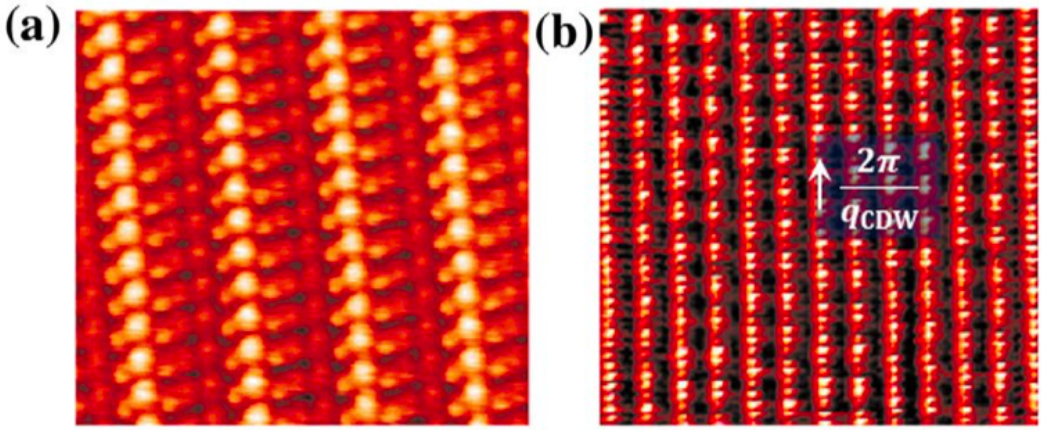

Figure 2.13: STM image of TTF-TcnQ showing (a) the normal state at 63 K and (b) the CDW state at 36,5 K [36].

2.9.2 Structure - reciprocal space

Variety of methods such as electron [38], X-ray [39], and neutron diffraction [40] might be used to determine the CDW superstructure through their sensitivity to the associated atomic displacement. Analysis of the diffraction patterns below T_{CDW} allows the determination of the nesting vector $q = 2k_f$ of the density-wave. Since these techniques allow large regions of reciprocal space to be quickly mapped out, they are useful in determining k_f.

To precisely measure the local displacement of atoms, X-ray spectroscopy can be used. Signs of CDW in each material can in that case be seen in "superstructure"-smaller Bragg peaks away from the nuclear Bragg peaks which appear at the T_{CDW} (Fig. 2.14)

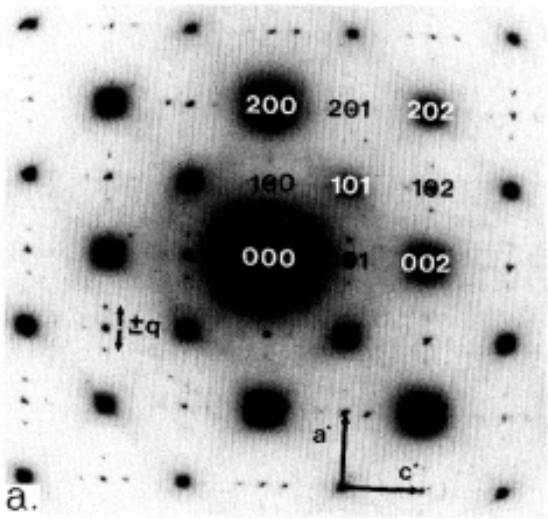

Figure 2.14: Superlattice Bragg peaks (smaller black circles) around a lattice Bragg peak (big black circle) in the $SmTe_3$ compound. [42].

These are a few examples of experiments used to identify and characterize the charge density waves. It should be noted that the CDW order affects the lattice, the electrons, as well as the Fermi surface. Thus, it has signatures in a wide variety of physical properties.

2.9.3 Electronic structure

Angle resolved photoemission spectroscopy enables the measurements of the electronic bend structure from where the CDW's energy gap and its temperature dependence can be determined. Moreover, from the measured the band structure and the Fermi contour the electronic susceptibility can be calculated [44]. Such complementary measurements reveal whether the CDW is driven by Fermi surface nesting or something else. Band-backfolding below T_{CDW} at the newly formed Brillouin zone boundaries can also be observed in ARPES measurements [37].

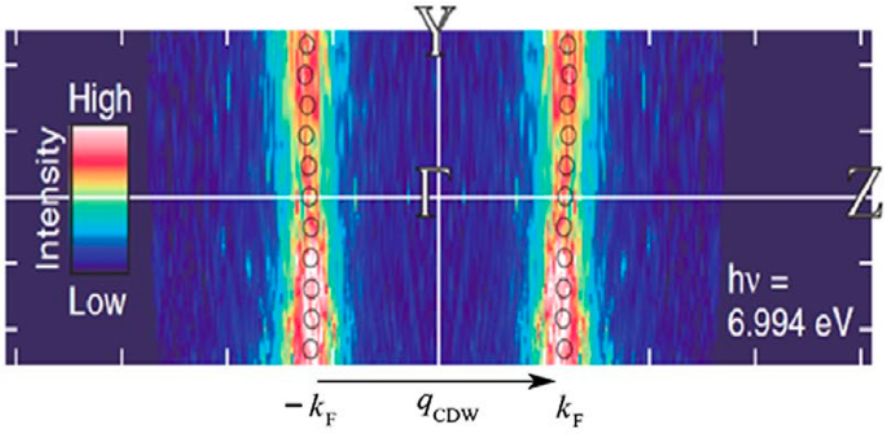

Figure 2.15: ARPES intensity mapping at E_F of TTF-TcnQ at 60 K, showing a clear quasi 1D Fermi surface from which nesting vector is determined [37]

2.9.4 Experimental tools used

In this thesis, we focused on research of CDW phenomenon with two experimental methods: First, the $BaNi_2As_2$ samples were characterised through resistivity measurements using the Physical Property Measurement System (PPMS). The goal of these measurements was to check for the behaviour of the material at low temperatures while being exposed to outer magnetic field. Then, the time-resolved optical-spectroscopy was employed to characterize the charge correlations in $BaNi_2As_2$, determine the cause of the observed periodic lattice distortion at low temperatures as well as to confirm and study the evolution of potential CDW collective modes. The application of these methods and results of their measurements are presented in Chapter 4. and Chapter 5.

Chapter 3

3. Barium nickel arsenide

3.1 About the compound

Barium nickel arsenide, $BaNi_2As_2$, is a non-magnetic structural homologue of the high temperature superconductor $BaFe_2As_2$ in which all the Fe cations are replaced by Ni. Since Fe and Ni are ambient temperature ferromagnets and many Fe and Ni compounds show magnetism, it is plausible to expect that Ni can fill in the role of Fe in these compounds [8].

Compared with the FeAs-based compounds, the NiAs-based systems were much less studied. Although the Ni-pnictide superconductors share the same structure type as Fe pnictides, the superconducting transition temperatures are much lower, and never exceed 5 K, even upon doping [12]. Nevertheless, a first-order structural phase transition at Ts = 137 K, and a superconducting transition at Tc = 0.7 K is found for $BaNi_2As_2$ compound. To date, no evidence for magnetic transition was reported [15].

The band structure of $BaNi_2As_2$ is similar to that of of $BaFe_2As_2$, except for the Fermi level, which is shifted up due to the higher valence electron count in Ni^{2+}. Hence, with a larger Fermi surface and higher carrier density, $BaNi_2As_2$ has remarkably different electronic properties than $BaFe_2As_2$. This suggests that the mechanism of superconductivity in (a dopped) $BaNi_2As_2$ is different from the Fe-based compounds [8]. The diffraction studies on $BaNi_2As_2$ demonstrated the existence of two types of periodic lattice distortions above and below the tetragonal to triclinic phase transition, suggesting charge-density-wave (CDW) order to compete with superconductivity [14].

3.2 Crystal structure

Recently, the crystal structure of $BaNi_2As_2$ was determined, and the structural phase transition from a high-temperature tetragonal phase to a low-temperature triclinic phase was established [15]. Based on the bond length examination, it was found that the As-As distance along the *c* axis increases at the transition from *3.553 Å* to *3.584 Å*, while within *a-b* plane, the Ni ions change from a square lattice to zigzag chains, where short Ni-Ni bonds *(2.8 Å)* are separated by longer Ni-Ni distances *(3.1 Å)*. The bonding is of a complex anisotropic character [10]. $BaNi_2As_2$ crystallizes in the tetragonal structure - space group *I4/mmm* and undergoes a structural distortion below approximately 135K. Theoretical work has also suggested that the zigzag chain structure in the triclinic distortion is driven by orbital ordering, explaining the lack of magnetic order [14].

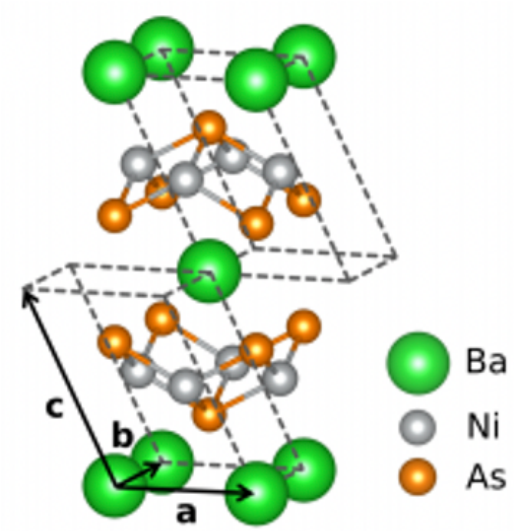

Figure 3.1: Crystal structure showing the triclinic unit cell (gray dashed lines) and basis vectors (black arrows) [14].

Tetragonal structure		Triclinic structure					
a (Å)	c (Å)	a (Å)	b (Å)	c (Å)	α (°)	β (°)	γ (°)
4.142(4)	11.650(3)	4.21(3)	3.99(2)	6.31(1)	105.2(3)	108.6(2)	89.3(4)

Table 3.1: Structure parameters and transition temperatures of $BaNi_2As_2$. Tetragonal lattice parameters are measured at room temperature and triclinic parameters at 50 K [8].

Fig. 3.2 illustrates the evolution of the structure observed by selected tetragonal and triclinic Bragg reflections in the H-K plane, at various temperatures. *(H, K, L)$_{tet}$* and *(H, K, L)$_{tri}$* are used to denote reciprocal space locations in tetragonal and triclinic units. In that case they are *(0, 0, 14)$_{tet}$* and *(0, 0, 7)$_{tri}$*, respectively. Refined lattice parameters are given in Table 3.1. As the sample is cooled, the intensity of the *(0, 0, 14)$_{tet}$* reflection decreases abruptly at $T_{tri} = 136K$. The *(0, 0, 7)$_{tri}$* peak appears, and its intensity grows rapidly below a narrow temperature range where the two peaks coexist. This observation supports previous claims that this transition is weakly first order [26].

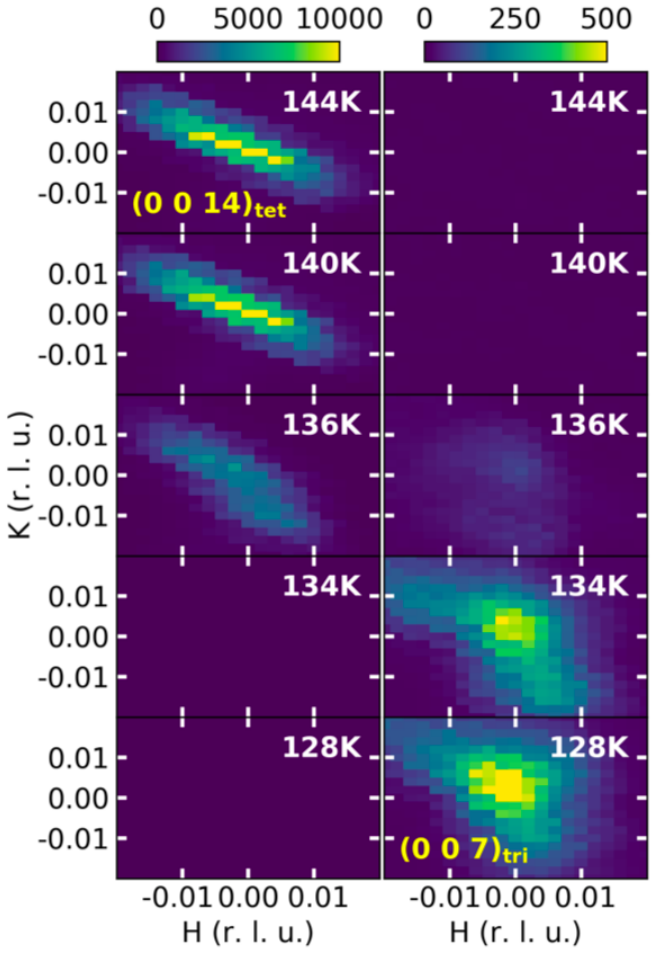

Figure 3.2: Evolution of the tetragonal to triclinic phase transition at given temperatures [8].

3.3 Key electronic properties

3.3.1 Band structure

The band structure of $BaNi_2As_2$ is similar to that of $BaFe_2As_2$ and shows a pseudogap between a manifold of six heavy *d* electron bands, and four lighter *d* bands (six *d* electrons per Ni). Unlike $BaFe_2As_2$, $BaNi_2As_2$ contains two more valence electrons. This causes the Fermi level to shift higher up from the pseudogap to the bands with higher dispersion *E(k)*, but lower density of states as a result of increased electron concentration. Hence, $BaNi_2As_2$ has a large multi-sheet three-dimensional Fermi surface (Fig. 3.4), in contrast to the small surfaces in the Fe-based superconductors [8].

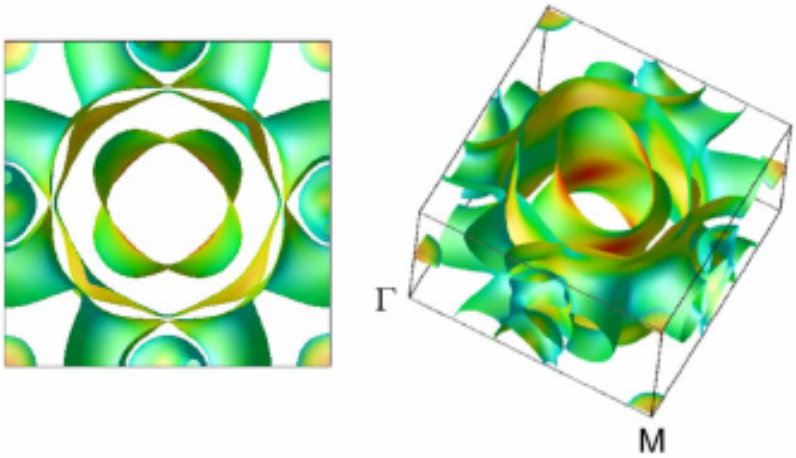

Figure 3.3: Calculated local-density approximation Fermi surface of $BaNi_2As_2$, without spin polarization [8].

Theoretical calculations show that $BaNi_2As_2$ phases adopt remarkably different electronic structure compared to $BaFe_2As_2$ owing to higher valence electron count in Ni than in Fe. The phonon spectrum and the strength of the electron-phonon coupling are consistent with a classification of this material as a conventional phonon-mediated superconductor, with a very small average electron-phonon coupling constant $\lambda_{ep} = 0.16–0.24$ [8].

3.3.2 Conductivity

$BaNi_2As_2$ exhibits a first-order structural transition at 130 K. Understanding this structural transition is a crucial step toward understanding the electronic properties of the material. Previous studies [8,10] revealed that $BaNi_2As_2$ is a good metal with high plasma frequency. By lowering the temperature across the transition, part of the spectral weight from conducting electrons is removed and shifted to high energies. The phase transition leads to a small reduction of conducting carriers. This reduction is caused by the removal of the states from the some of the Fermi surfaces, predominantly from the As-As bonding and Ni-As antibonding [10].

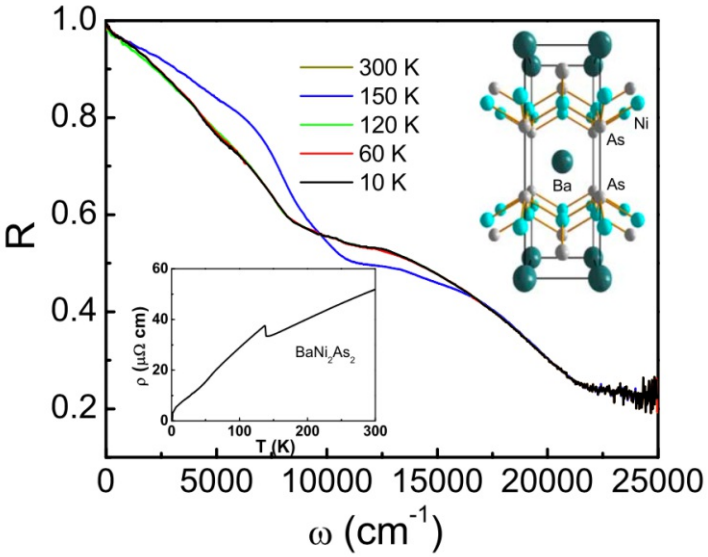

Figure 3.4: Reflectance curves up to 25000 cm^{-1} (~ 3 eV) at different temperatures. Upper inset shows the crystal structure. Lower inset shows the T-dependent dc resistivity [10].

3.3.3 Superconductivity & CDW

$BaNi_2As_2$ displays superconductivity below $T_c \approx 0.65\ K$ with no magnetic order reported down to the lowest temperatures [15]. Recent X-ray diffraction studies suggested two distinct charge-density-wave (CDW) orders, above and below T_S respectively [8]. What is particularly striking, is the observed six-fold enhancement of T_c and a giant phonon softening in phosphorus doped $BaNi_2As_2$ at the doping levels where the structural transition is completely suppressed [16]. The observed correlation between the enhancement of superconductivity and the increase in nematic fluctuations, may suggest a charge-driven electronic nematicity in $BaNi_2As_2$ [17]. However, until now, optical studies showed no signatures of the CDW-induced optical gap [10,13].

3.4 Growth method

A series of high-quality platelet-like single crystals of $BaNi_2As_2$ with typical dimensions of $2\times2\times0.5\ mm^3$ have been grown with self-flux method by Dr. Amir-Abas Haghighirad at KIT [16]. The self-flux growth is conceptually similar to the growth from an aqueous solution, but in such a case the solution contains only the crystal constituents, albeit with a different composition than that of the resultant crystal [15].

The self-flux growth was chosen for several reasons:

- The material melts incongruently
- The vapour pressure of arsenic is high at the required growth temperatures and is kept low during the flux growth.
- Stable secondary phases are prevented.

For the growth process, a slow cooling rate of 1 K/h was used. Different cycles of cooling and reheating protocols were followed to re-dissolve small crystallites which form in the initial state of cooling across the solidification temperature. For crystals of larger dimension, the linear growth rate should be always kept below the maximum stable value. In this way, it is possible to grow high-quality single crystals of $BaNi_2As_2$ [15].

The sample crystals are brittle, gray and shiny. Contact with air or moisture causes their decomposition. To prevent the decomposition, the crystals were stored in vacuum and were appropriately protected from the atmosphere when performing measurements.

Figure 3.5: Single crystalline samples of $BaNi_2As_2$.

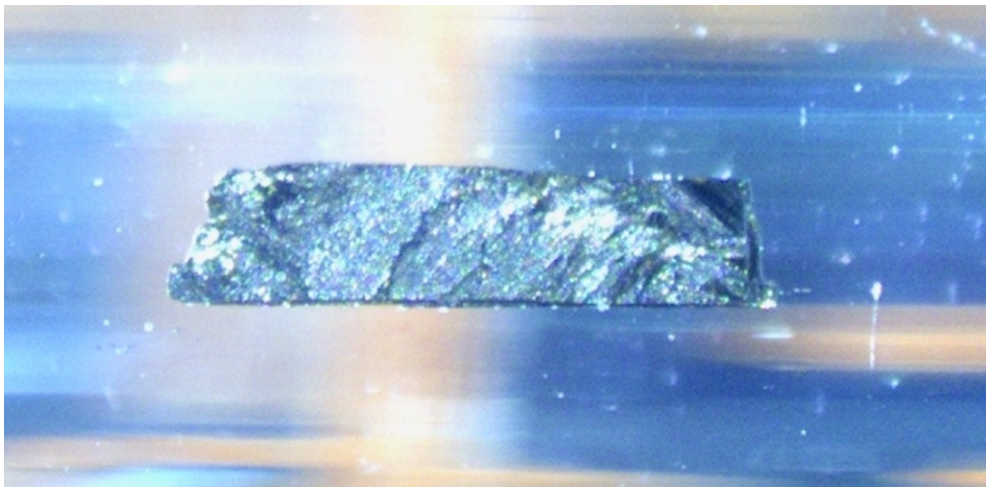

Figure 3.6: Magnification of a $BaNi_2As_2$ single crystal used for electronic transport measurements.

Chapter 4

4. Material characterization of $BaNi_2As_2$

4.1 Brief overview

Once the chemical composition of $BaNi_2As_2$ had been confirmed, the physical properties were further characterized. Since many of the ordering phenomena in condensed matter physics were discovered using the electronic transport measurements, DC resistivity measurements were performed to characterize the metal to insulator transition, and to verify the transition temperature [68]. In a new material, the first indication of a CDW usually comes from an anomaly in resistivity, specifically, in a form of kinks or sudden increase of resistivity [67]. The temperature dependent resistivity measurements often give the first indication, that material is susceptible to the CDW formation. In some cases, the phase transition can also be confirmed by measuring the magnetic susceptibility or heat capacity across the CDW-transition.

Within the framework of this thesis, the single crystals of $BaNi_2As_2$ were oriented using Laue diffraction method, and subsequently the planar resistivity measurements (in the *a-b* crystallographic plane) were performed to establish the transition associated with the CDW transition. Furthermore, magnetic field of 9 T was applied to verify the influence of such field on the transition temperature.

4.2 Crystallography of $BaNi_2As_2$

4.2.1 Laue Diffraction

Laue diffraction is used for the determination of the orientation of a crystal when the lattice symmetry is known, and it consists of detecting spots that originates form the Laue diffraction pattern [68].

Laue diffraction pattern, first detected by Max von Laue, corresponds to a regular array of spots that can be recorded, e.g., by a photographic emulsion, which results from X-rays scattered by certain groups of parallel atomic planes within a crystal. When a crystal is exposed to a multi-wave beam of X-rays, certain wavelengths might be scattered in-phase from a group of atomic planes, so that intense spots are observed on a film. These spots are centred around the central image of the direct beam, which passes through undeviated [68].

The diffraction pattern can be explained by the "von Laue condition", which establishes the relationship that exists between the occurrence of constructive interference and the distance of the atoms within a crystal. The condition is expressed by the formula [68]:

$$d * \Delta K = 2\pi m \qquad (4.1)$$

where d is the *inter-atomic distance* and ΔK is the *difference between the incident and the diffracted wave vector*. This condition can be expressed by introducing the concept of *reciprocal lattice vectors* G [68]:

$$\Delta K = G \qquad (4.2)$$

Expressed in this way, the Laue condition implies that in an elastic collision, the momentum transferred to a crystalline lattice is equal to a vector of the reciprocal lattice. The spots present in a Laue diffractogram correspond to the reflections (constructive interferences) produced by a set of crystallographic planes. The Laue image is therefore a direct representation of the reciprocal lattice, where each spot corresponds to a point of the reciprocal lattice, which in turn correspond to a set of crystallographic planes. This method requires the use a polychromatic beam to simultaneously satisfy the von Laue condition for a number of families of planes.

Polychromatic beam is a beam, which contains a wide range of wavelengths that potentially satisfy the conditions of constructive interference [68]. Laue diffraction can be performed in two configurations: Transmission or Back-reflection, as presented in Fig. 4.1.

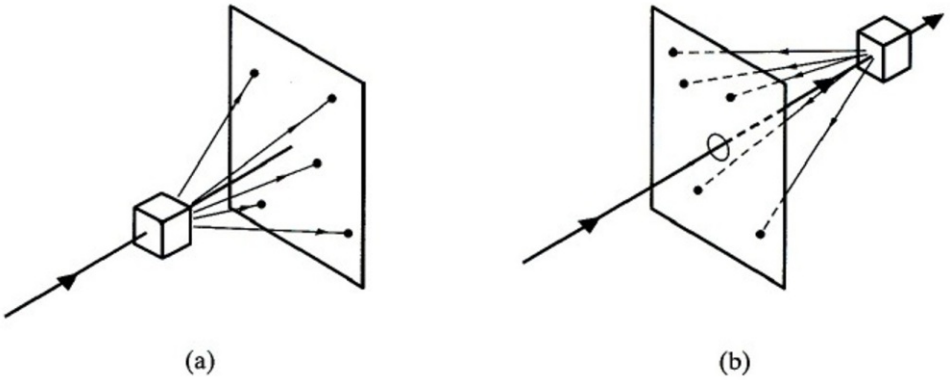

Figure 4.1: Single crystal Laue diffraction in (a) Transmission and (b) Back-reflection configuration [68].

The image obtained is linked to the structure of the crystal lattice and its symmetry properties. The spots, arranged along the ellipses, show the intersection of the diffraction cones with the plane of the photographic plate [68].

4.2.2 Experimental setup & Measurement procedure

Laue diffraction Back-reflection technique was used to determine the crystallographic orientation of $BaNi_2As_2$. Here the sample is placed on a goniometer in a well-collimated beam of X-rays, with the 2D detector positioned between the crystal and the X-ray source. The X-rays are diffracted by each set of lattice planes with a wavelength that obeys the Bragg's law, and the diffraction pattern is registered by the detector. The schematic of the technique is shown in Fig. 4.2. Furthermore, the experimental setup of a Laue diffractometer with its components, used to determine the structure of $BaNi_2As_2$ crystal lattice, is presented in Fig. 4.3.

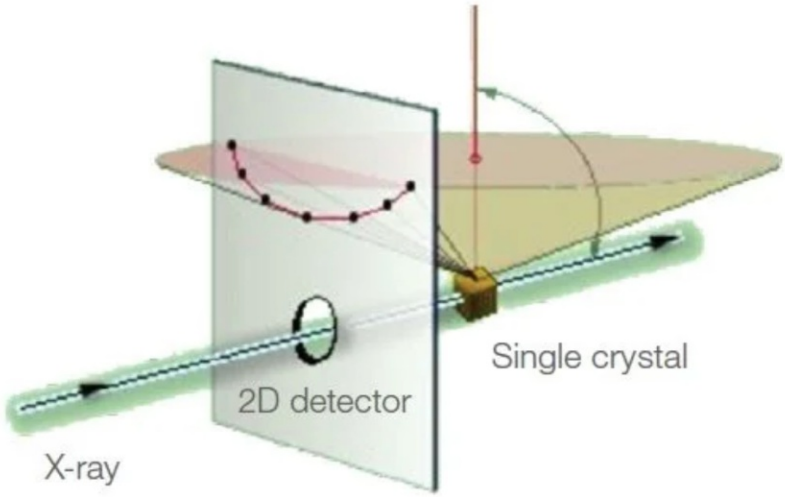

Figure 4.2: Laue diffraction in Back-reflection configuration, where X-ray beam passes through the 2D detector, being reflected from the crystalline sample afterwards [45].

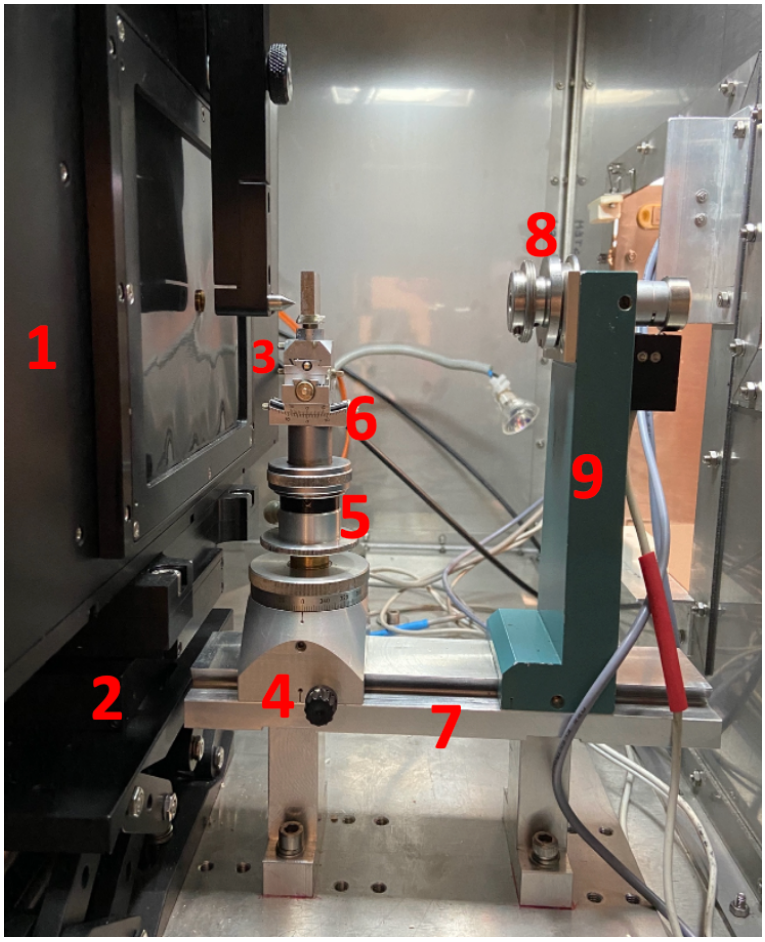

Figure 4.3: Experimental setup of a Laue diffractometer with its components.

1 – CCD X-ray detector with the X-ray source behind it

2 – Detector adjustable holder

3 – Pin for the sample alignment

4 – Goniometer stage

5 – Y-Z stage

6 – Goniometer

7 – Optical rail

8 – Alignment camera

9 – Beam stop

After the $BaNi_2As_2$ sample was mounted on a holder and placed in the X-ray beam, the single-crystal x-ray diffraction data were collected for 5 minutes to obtain a high-resolution image of the diffraction pattern.

4.2.3 Results

Figures 4.4 and 4.5 show the Laue diffraction pattern and the sample for which the pattern was recorded, respectively. The edges of the sample are oriented along the main crystallographic axes *a* and *b*, which are equal in the tetragonal symmetry of $BaNi_2As_2$ crystal at room temperature. The surface corresponds to the surface of the $BaNi_2As_2$ planes (see Fig. 4.5).

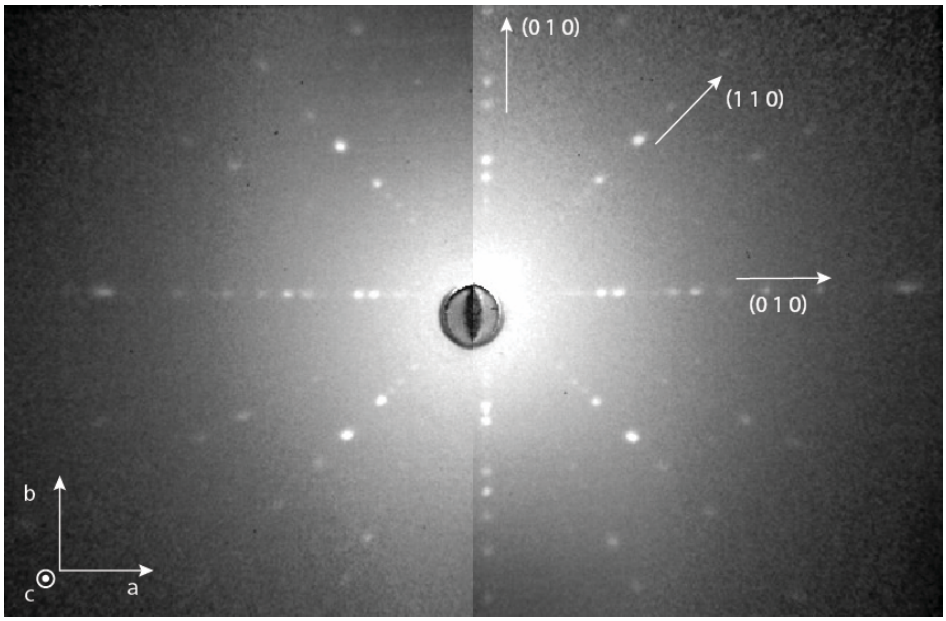

Figure 4.4: Laue Diffractogram of a $BaNi_2As_2$ crystal. The orientation of the crystallographic axes corresponds to the sample orientation shown in Fig. 4.5.

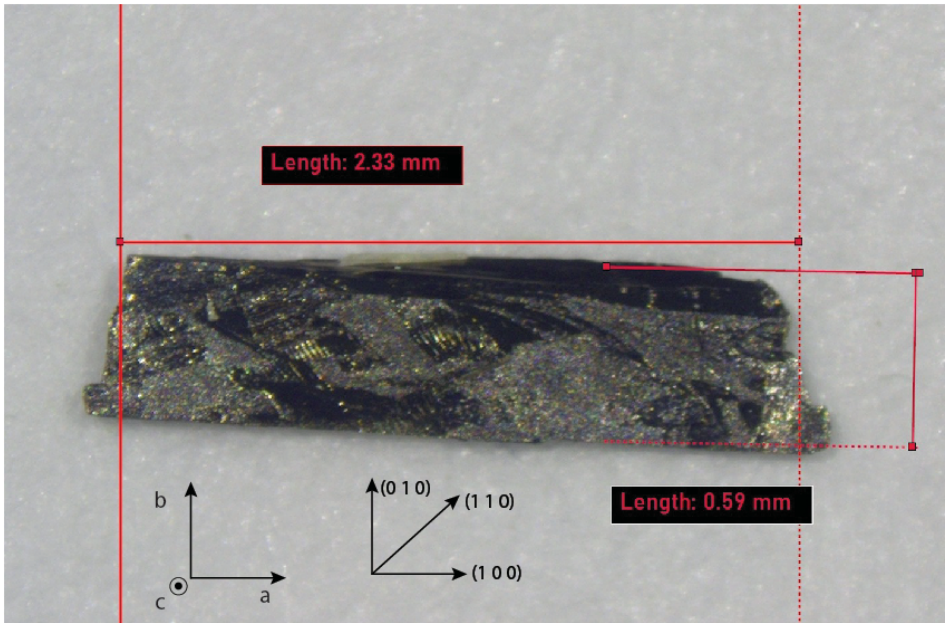

Figure 4.5 $BaNi_2As_2$ single crystal under the microscope.

4.3 Resistivity of $BaNi_2As_2$

4.3.1 Four-point measurement method

The four-probe method, also known as the Kelvin technique, is a primary technique for measuring resistance. It consists of four co-linear electrical contacts as shown in Fig. 4.6.

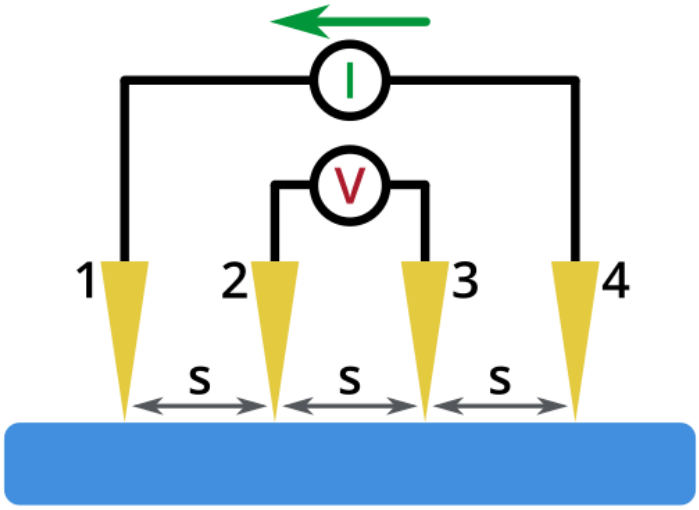

Figure 4.6: Illustration of a four-probe method. Blue colour depicts the measured sample [56].

Here, four metallic probe pins are attached to the surface of the specimen. While the current is applied on the outer two probes (1 and 4), the resultant voltage drop is measured between the inner two probes (2 and 3). In a specific case, when the probes centred on a very wide (lateral dimension $d >> s$) and very thin (thickness $t << s$) sample, the resistivity Rs can then be calculated using the equation [56]

$$Rs = \frac{\pi \, \Delta V}{\ln(2) \, I} \qquad (4.3)$$

4.3.2 Sample preparation

One of the most important aspects of the electronic transport measurement is the preparation of the electrical contacts on the sample. Good contacts should have a very small resistance (<1 Ohm), which minimise spurious effects, which can arise from a large capacitance.

Before contacts are attached, it is important to be attentive to the sample's geometry, which plays an important role in very anisotropic compounds, affecting importantly the accuracy of the resistivity estimation as well as the overall behaviour of the measured curves. Ideally, the sample should be a long rectangular cuboid with infinitesimally small contacts being placed at its ends. The smaller the contacts are in comparison to the sample's dimensions, the higher accuracy can be achieved. Also, the thickness of the sample should be constant along its length.

The contacts were made by attaching golden wires (with diameters of 20 μm) directly on the sample surface, using silver paint DuPont 4929. The gold wires were first immersed in the paint, then placed on the sample. As the solvent dries, the liquid paint forms a solid paste, adhering the wire to the sample.

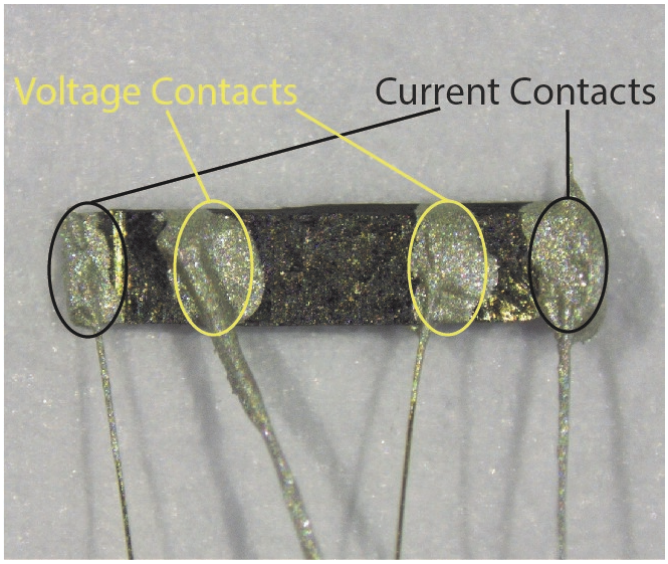

Figure 4.7: BaNi2As2 with attached contacts using silver paste technique.

Finally, contacted sample is attached onto the sample holder, the so called "interchangeable sample puck" (see Fig. 4.8), using GE varnish and cigarette paper, which can then be installed into the experimental setup.

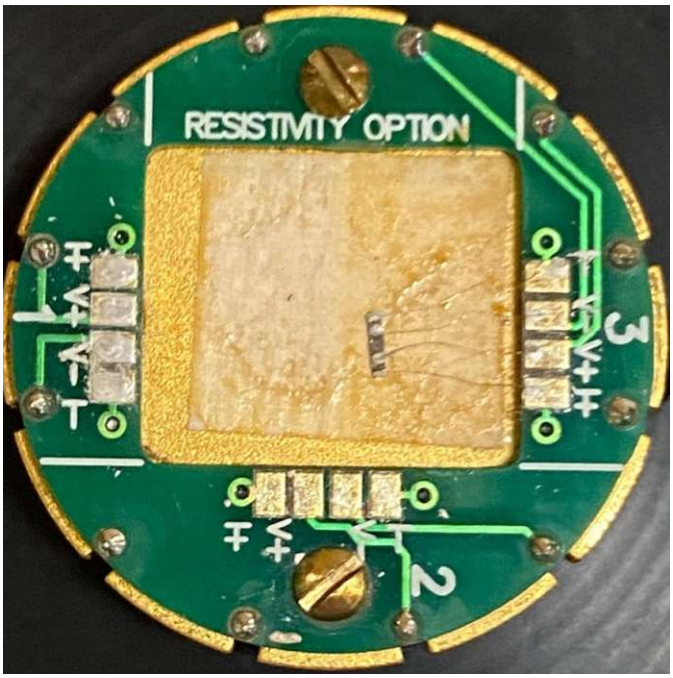

Figure 4.8: Contacted sample attached on the sample puck, prepared for resistivity measurements. Layer of a cigarette paper is right below it, glued on the puck with GE varnish to electrically isolate the sample from the puck.

4.3.3 Experimental setup & Measurement procedure

Resistivity measurements were performed using the Physical Properties Measurement System (PPMS) by Quantum Designs. The PPMS is an automated low-temperature and magnet system for the measurement of material properties like specific heat, magnetic AC and DC susceptibility and both electrical and thermal transport properties. In the ordinary set-up, temperature is controlled down to 1.8 K by pumping liquid ^{4}He into a sample pot. By precisely balancing the cooling power of the liquid helium, with the heat being supplied through a resistor, the PPMS can stabilize temperatures from 1.8 K to 320 K with 0.01 K accuracy.

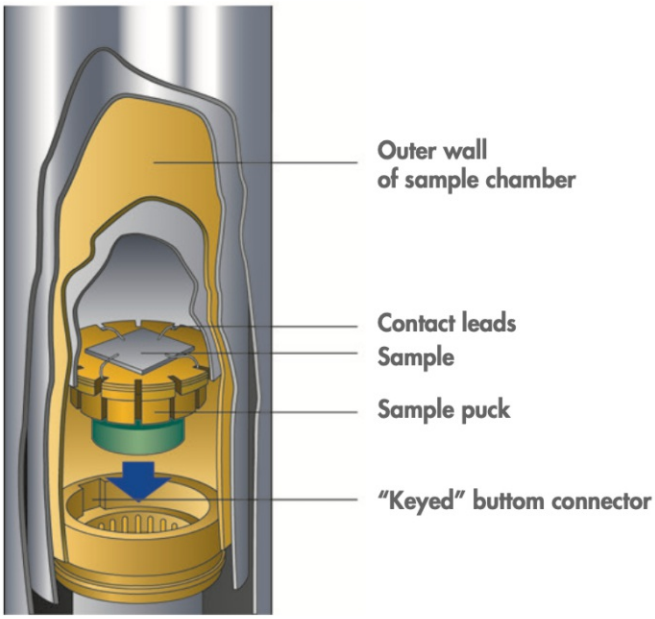

Figure 4.9: Breakdown of a PPMS sample chamber [60].

The base unit of the PPMS consists of a cryostat (see Fig. 4.11) with a superconducting magnet. The different measurement options can be employed by the use of different measurement inserts or sample holders (see Fig. 4.10.).

Figure 4.10: Different kinds of PPMS utility inserts [60].

Finally, the resistivity of $BaNi_2As_2$ was measured between the temperatures of 2 K and 285 K for both heating and cooling, at a rate of 1 K/min. The data were collected in the absence of magnetic field and in the field of 8 T.

Figure 4.11: PPMS consisting of a cryostat (black dewar left) and a controller (right).

4.3.4 Results & Analysis

In this section, a few selected datasets will be presented, namely: resistivity measurement without magnetic field, resistivity measurement under the magnetic field of 8 T as well as the comparisons of heating and cooling processes under both configurations.

Fig. 4.12 presents the resistivity of $BaNi_2As_2$ upon heating (red) and cooling (blue) in the temperature range from 2 K to 285 K, without the magnetic field.
As expected, resistivity rises with temperature upon heating and falls upon cooling, throughout measurement, with a characteristic feature around 137 K. Here, resistivity experiences a short, but sharp and yet significant drop (while heating) and rise (while cooling).

This anomaly is a sign of a first order structural transition of a $BaNi_2As_2$, where the crystal lattice changes symmetry from tetragonal (above ~130 K) to triclinic (below ~130 K). This finding in our measurement is in a good agreement with findings reported in literature [7,11] and is also a good indicator of the potential formation of the CDW order [67].

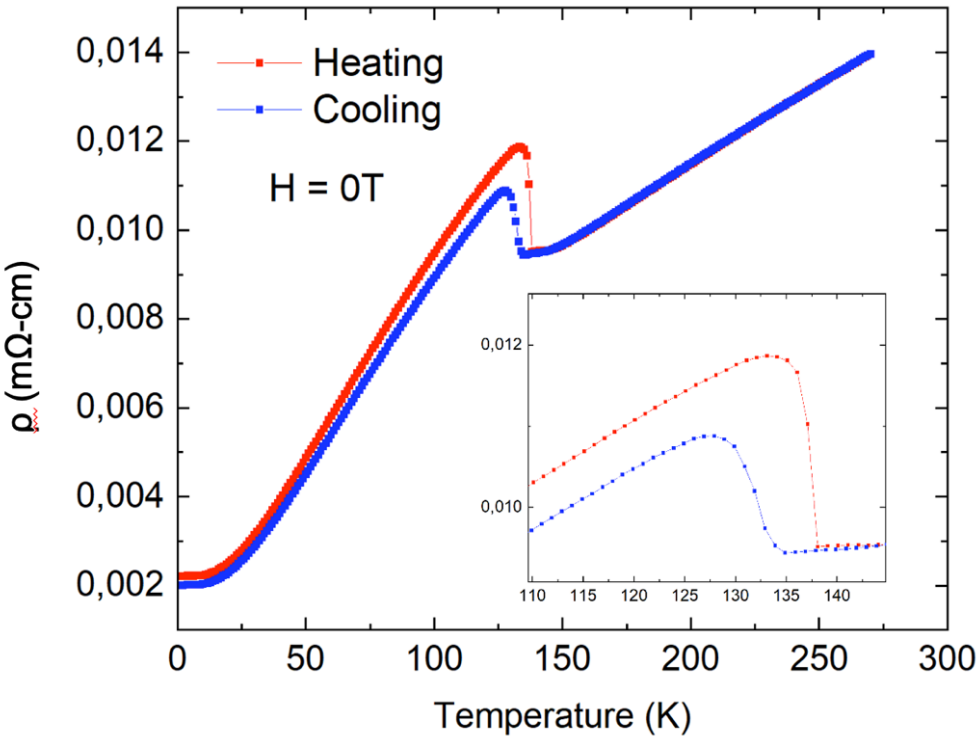

Figure 4.12: In-plane resistivity of $BaNi_2As_2$ measured without magnetic field. The inset demonstrates the thermal hysteresis at the transition.

Fig. 4.13 presents the resistivity of $BaNi_2As_2$ upon heating (red) and cooling (blue) between 2 K and 285 K, with the magnetic field of 8T. As it can be seen from the data, there is no apparent difference between the measurements with and without the magnetic field. Such observation indicates that $BaNi_2As_2$ is indeed a non-magnetic material [8]. First order structural transition again appears at ~130 K, just as in the data set collected without the magnetic field. In both cases, the thermal hysteresis is approximately $\Delta 5$ K. This observation is again in a good agreement with the findings reported in literature [7,11].

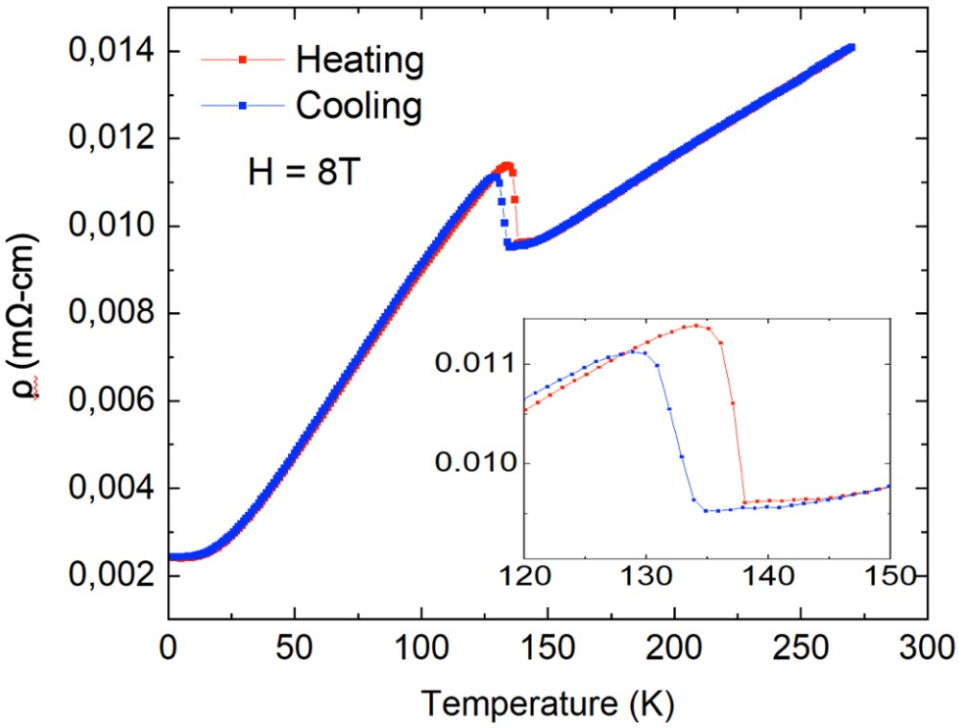

Figure 4.13: In-plane resistivity of $BaNi_2As_2$ measured with magnetic field. The inset demonstrates the thermal hysteresis at the transition.

Figures 4.14 and 4.15 compare the measurements performed in the presence and absence of the external magnetic field. The comparison was made for the data collected upon heating and cooling, respectively. This analysis shows that resistivity does not change significantly upon application of magnetic field. In particular, magnetic field does not shift the structural transition temperature. This additionally supports the non-magnetic character of $BaNi_2As_2$.

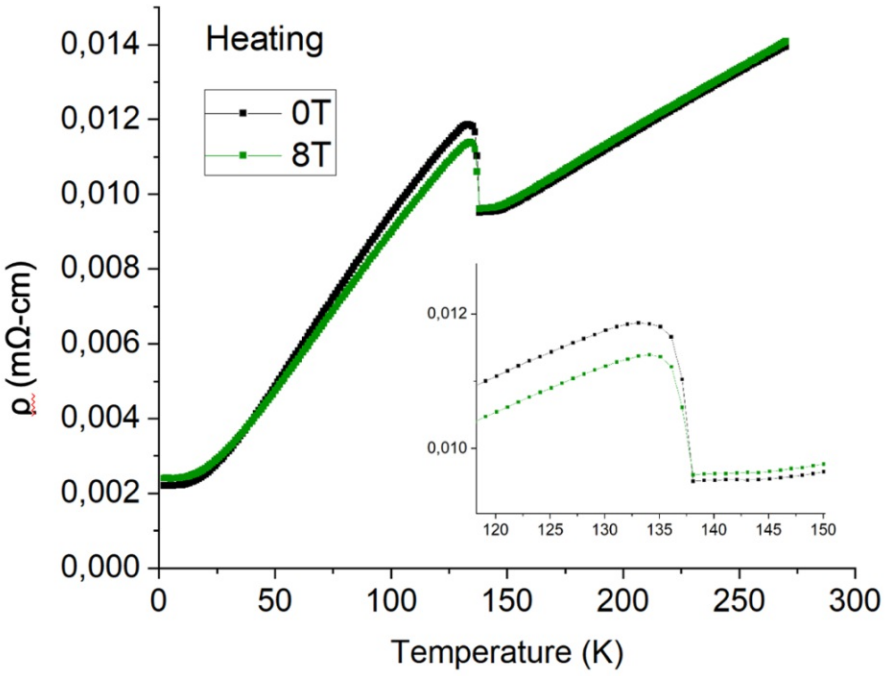

Figure 4.14: Comparison of in-plane resistivity of $BaNi_2As_2$ measured with and without magnetic field upon heating. The inset shows that the transition temperature while heating does not change as a function of field.

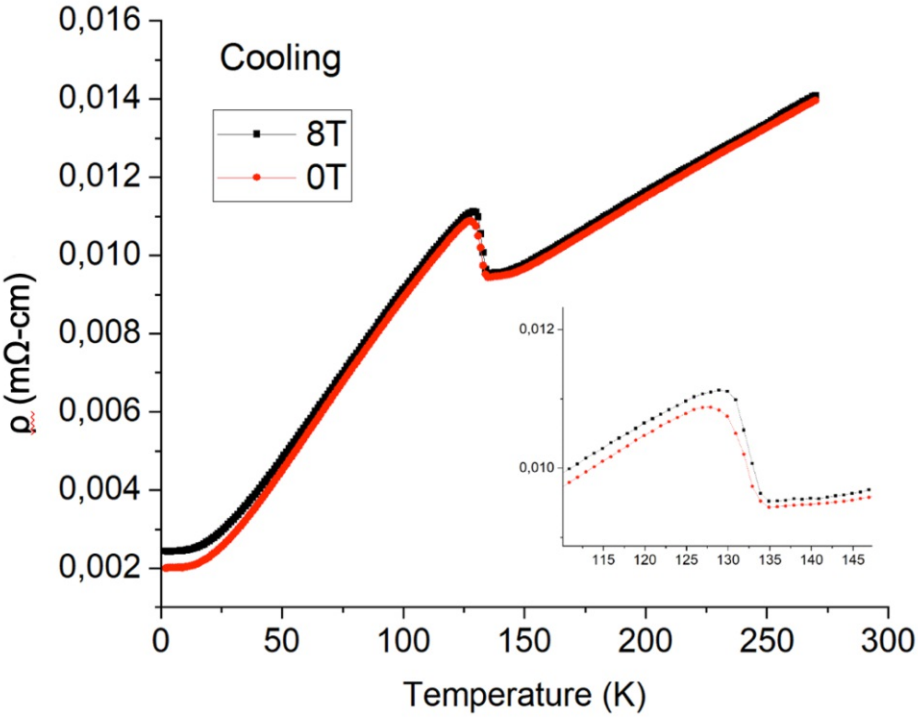

Figure 4.15: Comparison of in-plane resistivity of $BaNi_2As_2$ measured with and without magnetic field upon cooling. The inset shows that the transition temperature while cooling does not change as a function of field.

An important outcome from the resistivity measurements is a demonstration of the sharpness of the transition, which indicates that the sample is of a good quality and identification of a phase transition at around 137 K. This temperature is thus a good starting point to investigate the difference in character between the high-temperature and low temperature state [67], where the CDW state should be sought in the temperature range between 2 K and 150 K.

Although electronic transport measurements are extremely useful in providing the estimate for T_{CDW}, they do not confirm the formation of a CDW state. For example, such measurements cannot distinguish between charge and spin-density waves. Confirmation of the presence of a CDW order requires the observation of the periodic-lattice-distortion, observation of the energy-gap associated with the creation of a new Brillouin-zone, or direct observation of the charge modulation. Therefore, the $BaNi_2As_2$ was additionally investigated with time-resolved optical spectroscopy method, to gain further insights in the formation of the CDW states.

Chapter 5

5. Time-resolved optical spectroscopy of $BaNi_2As_2$

5.1 Brief overview

To verify that CDW collective modes are indeed the cause of the observed periodic lattice distortion at low temperatures in $BaNi_2As_2$, a careful study of these collective modes is required [9, 45, 46]. Method of femtosecond time-resolved optical spectroscopy, so called "pump-probe" optical spectroscopy has been applied for that purpose. With this method it is possible to observe interactions by abruptly perturbing the electronic distribution while keeping track of energy relaxation pathways and coupling strengths among the different subsystems [47]. Moreover, it has been demonstrated that pump-probe spectroscopy is particularly sensitive to low-energy $q \approx 0$ Raman-active collective modes in systems exhibiting CDW order [48]. The method offers spectral resolution up to 0.1 cm^{-1}, access to modes at frequencies down to the 100 GHz (3 cm^{-1}) and is suitable for investigation of inhomogeneous samples [49]. By analysing frequency spectrum of transient reflectivity and combining the information obtained from the temperature (T) and excitation fluence (F) dependence we were able to extract information about of density wave dynamics. By that we gained novel insights into the nature of the ground states [50].

5.2 Pump-probe optical spectroscopy

5.2.1 Basic principles

Numerous processes in nature, such as molecular vibrations, phonon absorption/emission and scattering phenomena, occur on a very fast time scale of the order of picosecond. To accurately measure ultrafast processes, the uncertainty in timing must be smaller than the time scale of the process, requiring temporal resolution of the order of 50 – 100 femtoseconds (10^{-15} s). One of the techniques that provides such time resolution is the pump-probe optical spectroscopy [11]. In this technique, an ultra-short laser pulse train is split in two; a pump beam, which is used to excite the sample, generating a non-equilibrium state, and a probe beam, which is usually weaker than the pump beam and is used to monitor the pump-induced changes in the optical properties (such as reflectivity or transmittivity) of the sample [52].

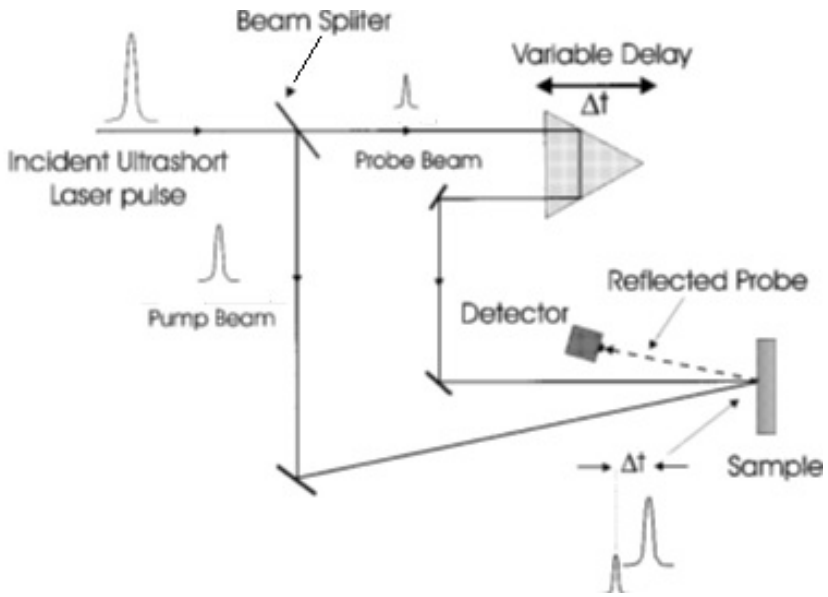

Figure 5.1: Typical pump-probe experimental set-up with main components [53].

At the first stage in performing the pump-probe measurements a beam splitter is used in order to divide a laser beam into the pump beam and the probe beam (Fig. 5.1). Pulses of both beams reach the sample through different optical paths and are thus delayed with respect to each other; the delay between the pulses can be varied by varying the optical path of one of the beams.

As the pump - probe spectroscopy is a tool to study dynamical processes, the physical system must be perturbed from an equilibrium state. This is accomplished through the pump pulse. The probe pulse records the optical properties state at a time-delay $d\tau$ given by [11],

$$d\tau = dX * c \qquad (5.1)$$

where dX is the (optical) path length difference between the pump and probe pulses and c is the speed of light. This is achieved by inserting a delay line into its path. The delay line consists of a precise motorized translation stage, with optical mirrors (retroreflector) mounted on it. The probe beam is measured with a detector after it has interacted with the sample (see Fig. 5.1) [11].

By such an approach one can study the time evolution of reflectivity and transmission, thereby obtaining the information of time evolution of the complex refractive index [53]. Using non-linear optical processes, the approach can be extended to a broad spectral range, with pump and/or probe sources ranging from THz to UV [71]. The pump pulse can be tuned in many ways including photon energy, intensity, polarization and the pulse duration in order to excite the sample.

5.2.2 Details of the used experimental set-up

A commercial Ti:Sapphire amplifier with repetition rate of 300 kHz, producing 50 fs laser pulses at λ = 800 nm (photon energy of 1.55 eV) was used as a source of both pump and probe pulse beams. The beams were impinging on the sample at near normal incidence, and were cross-polarized, in order to reduce the noise. The induced changes of an in-plane reflectivity R were recorded utilizing a fast-scan technique, enabling high signal-to-noise level [48]. The essential components of the experimental pump-probe setup are schematically outlined in Fig. 5.2.

The laser beam is first collimated in a telescope and is split in two (pump and probe) beams in a polarizing beam splitter (PBS). forming both pump and the probe beams, perpendicular to each other.

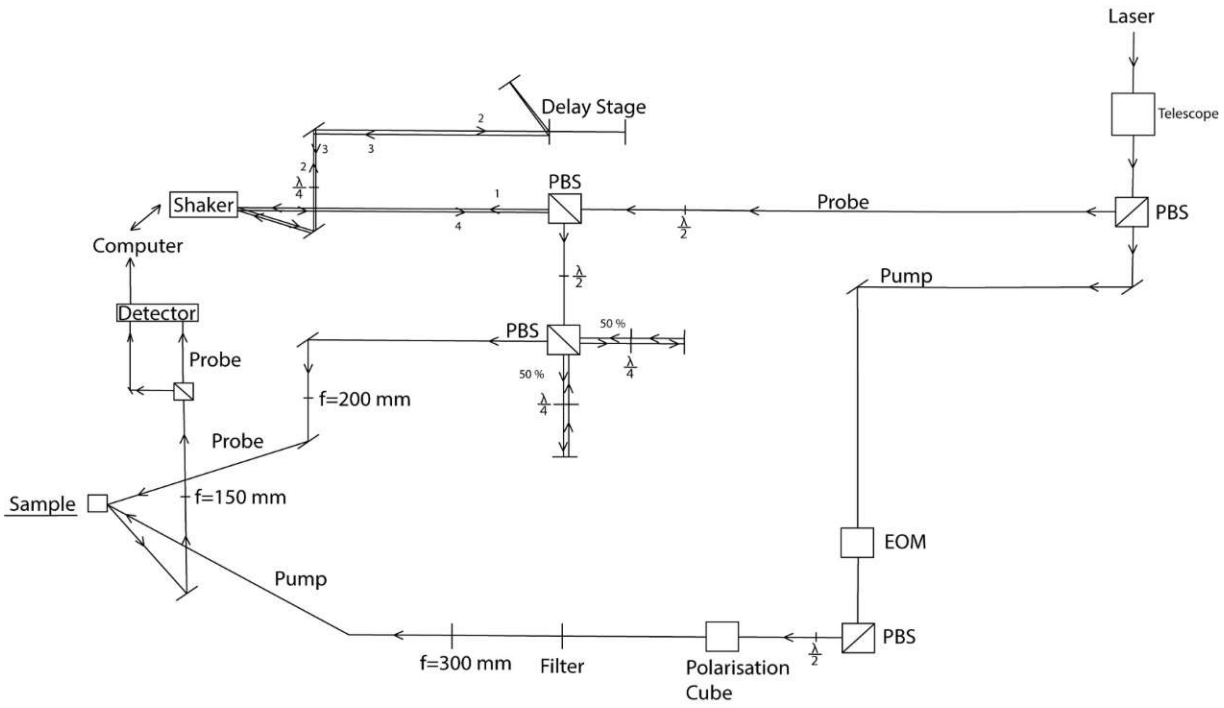

Figure 5.2: Schematic of the experimental optical pump-probe set-up.

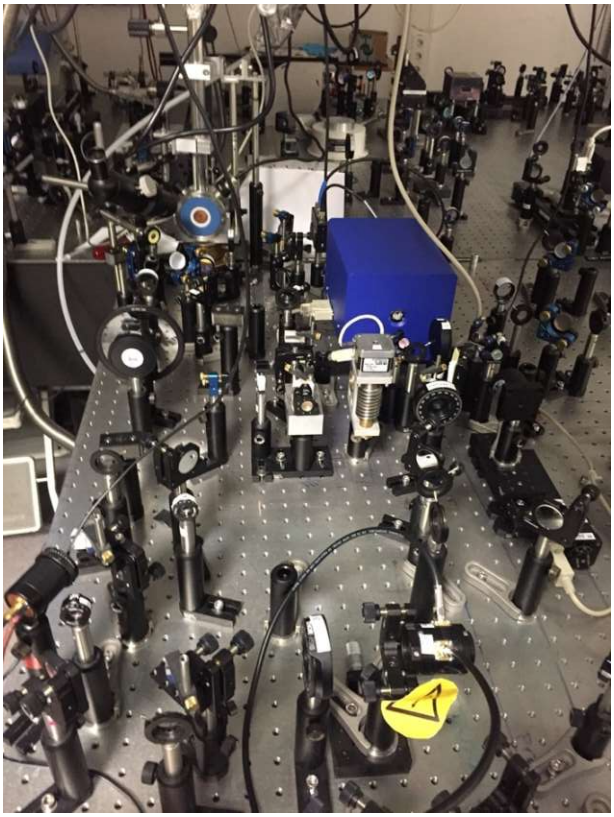

Figure 5.3: Experimental optical pump-probe setup in the lab.

The pump beam passes through the electro-optic modulator (EOM). The principle of operation of the EOM is that by applying electrical field to the EOM crystal, the induced birefringence causes rotation of the light polarization. In combination with a polarizer, the EOM is set to modulate the light beam by blocking every second optical pulse [64]. To achieve that, the timing of the EOM must be synchronised with the pulsed laser. This is achieved by the dedicated pulse generator triggered by laser output.

Next, the pump beam travels through the half-wave plate, marked with *λ/2,* followed by a polarizer. The half-wave plate rotates the polarisation and with that regulates the amount of the transmitted light through the polarizer. Thereby the pump fluence on the sample is adjusted. Power of the pump beam can further be varied by neutral density filters, before it is finally focused on a sample.

Meanwhile the probe beam goes through a setting of polarized beam splitters and half-wave plates, whose function is to provide a sequence of probe and reference beams for differential detection (details can be found in literature [72]). After that, the probe beam is directed into the combination of fast shaker (see section 5.2.3) and a mechanical delay stage used to control the time delay between the pump and the probe.

The mechanical delay stage is realised by a computer controlled linear stage on which a retroreflector (or combination of two mirrors) is mounted, where probe beam's optical path can be optionally prolonged to enable time delays in access on one nanosecond. An example of it is shown on the Fig. 5.4.

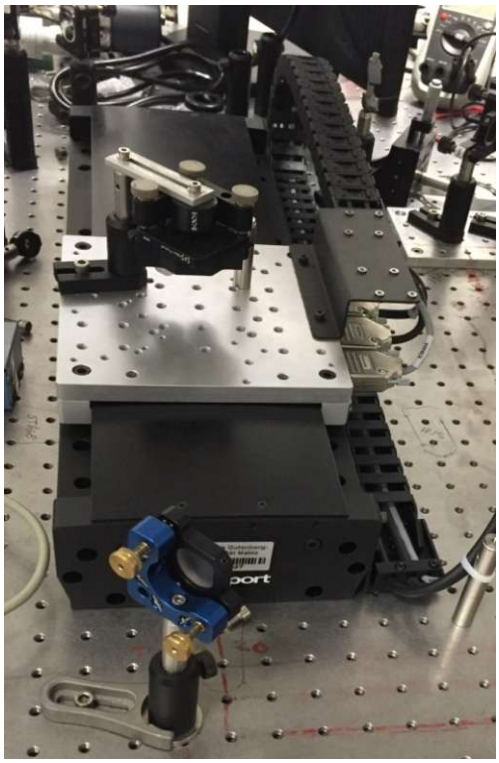

Figure 5.4: The delay stage.

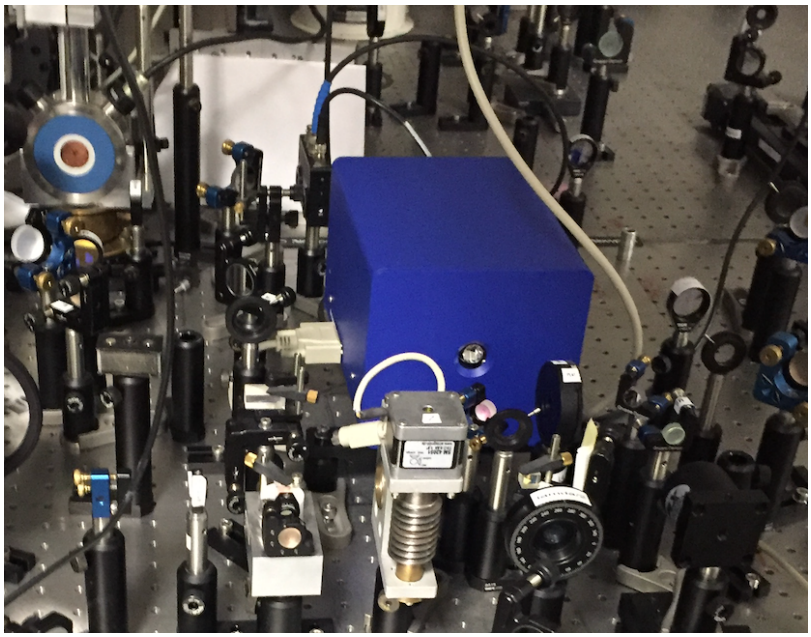

Figure 5.5: Shaker (blue box) as a part of the optical set-up.

Fast shaker (APE Scan Delay 150) is a mechanical vibrator that involves piston motion along one axis (see Fig. 5.5). A small retroreflector is mounted on the drive arm of a mechanical vibrator (therefore also known as shaker), which is powered by a signal generator. Generally, the amplitude of motion depends on both the frequency at which the shaker is driven, and the load mounted on the end of the drive arm. The APE Scan Delay 150 is normally operating at 10 Hz, providing up to 150 ps time delay (or 300 ps, in case of double pass configuration).

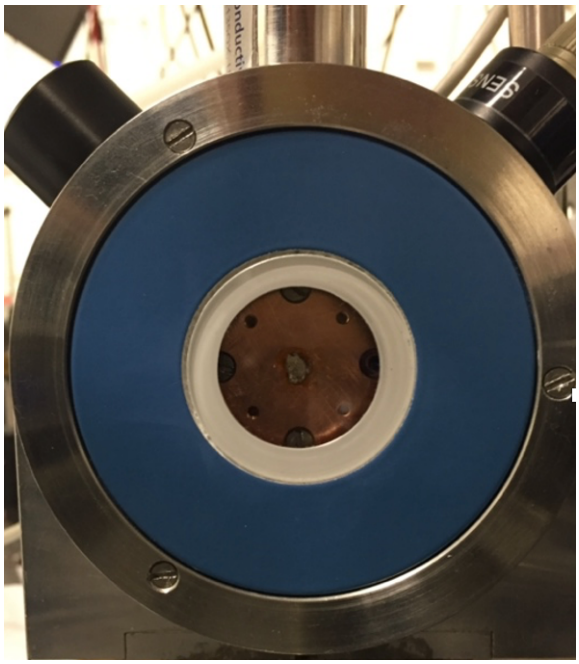

Figure 5.6: $BaNi_2As_2$ sample mounted on the mechanical holder, inside of a cryostat.

Following the different optical paths, the pump and the probe beams are finally focused on the same area of the sample. The spot size of the pump/probe beam in the focus was roughly 80/50 μm. It is of significant importance that probe beam falls completely within the area of the pump. In order to accomplish spatial alignment, a microscope was used to visually align the spots, and achieve best spatial overlap.

The sample was placed in the cryostat, which was mounted on an x-y-z translation stage to allow movements of the sample in different directions and by that, to probe different spots on the sample surface (Fig. 5.6). The pump and the probe beams are reflected from the sample's surface. The change in the reflectivity of the probe $\Delta R/R$ is measured with a photodetector (Fig. 5.7).

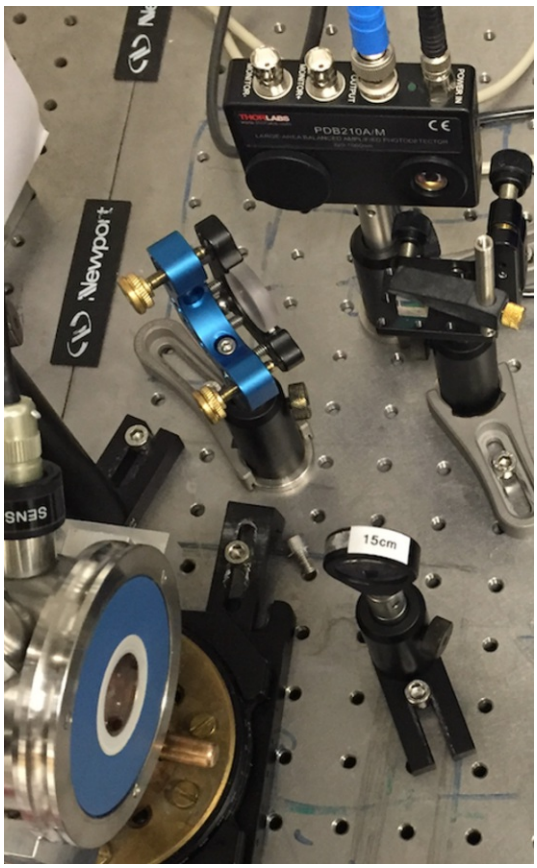

Figure 5.7: $BaNi_2As_2$ sample inside of a cryostat (left). After scattering on the sample, the beam is reflected to the photodetector (top).

5.2.3 Fast-scan

During the measurements, the so-called fast-scan technique has been utilized. Here, the time-delay between the pump and the probe pulse is controlled by a fast-scan shaker (APE Scan Delay 150). In terms of signal/noise ratio this method is preferred over the conventional lock-in technique using a combination of a modulator and lock-in amplifier. General femtosecond pump-probe spectroscopy technique uses lock-in method to measure the optical properties of samples. However, this method is susceptible to slow drifts of the laser. Fast signal averaging using the fast scan, in combination with pump-modulation, provided by the EOM, has been proven as a best combination using the high-repetition rate laser amplifier [72]. Hence, the use of a fast-scanning system drastically improves the signal-to-noise ratio [65].

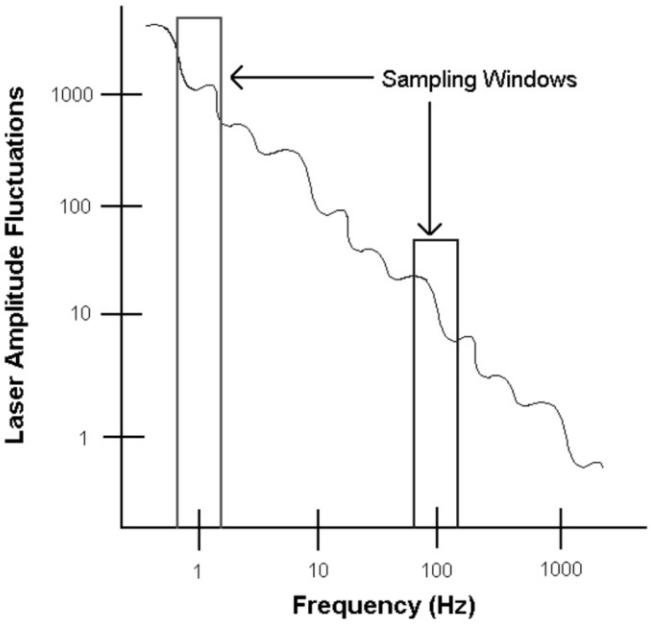

Figure 5.8: Typical frequency dependent laser amplitude fluctuations [65].

In our experiment, the differential detection scheme (the signal from the beam reflected from the sample's surface is subtracted from the reference beam) and averaging on the oscilloscope have been used to achieve high signal-to-noise ratio. The shaker operated at a frequency of 10 Hz with maximum displacement corresponding to the time delay of 100 ps.

5.3 Sample preparation & Measurement procedure

Single crystals of $BaNi_2As_2$ with typical dimensions $2\times2\times0.5$ mm^3 were grown by self-flux method as described in Chapter 3.4. Prior to the measurement, the samples were mechanically freed from the flux and cleaved with a scotch tape along the ab-plane. This procedure of removing the surface layer is required since the compound oxidizes in air. Afterwards, samples were glued on the cupper holder with General Electric Varnish (GE Varnish), to achieve better thermal conductivity at low temperatures. Finally, they were mounted on an optical cryostat, where they were kept in the vacuum during measurements.

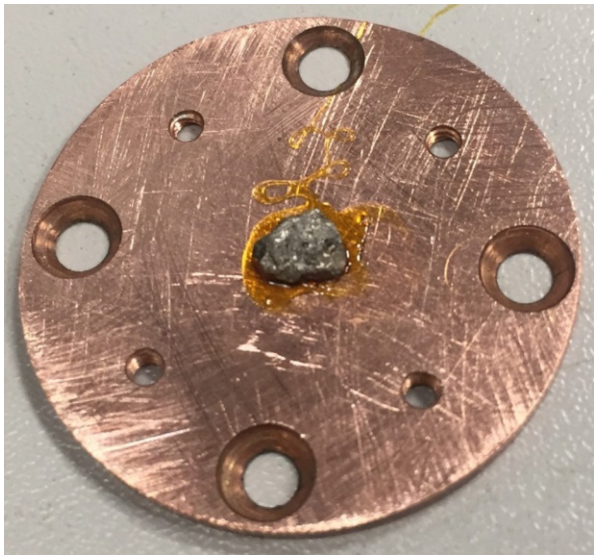

Figure 5.9: Sample of $BaNi_2As_2$ (grey) glued onto the metallic holder with GE Varnish.

5.4 Results & Analysis

During the pump-probe optical spectroscopy measurements of $BaNi_2As_2$ the temperature- and fluence was varied and photoinduced reflectivity was recorded. The fluence of the pump beam was varied between 0.1 and 4 mJ/cm^2 while the probe fluence was about 30 µJ/cm^2. Finally, the measured data has been analysed by use of OriginLab software.

Figure 5.10 shows the T-dependence of photoinduced transient reflectivity *R/R(t),* recorded upon heating the sample from 10 K to 146 K at a constant fluence of F = 0.4 mJ/cm^2. Here, clear oscillatory response is observed up to 146 K with a strong decrease above this temperature [69].

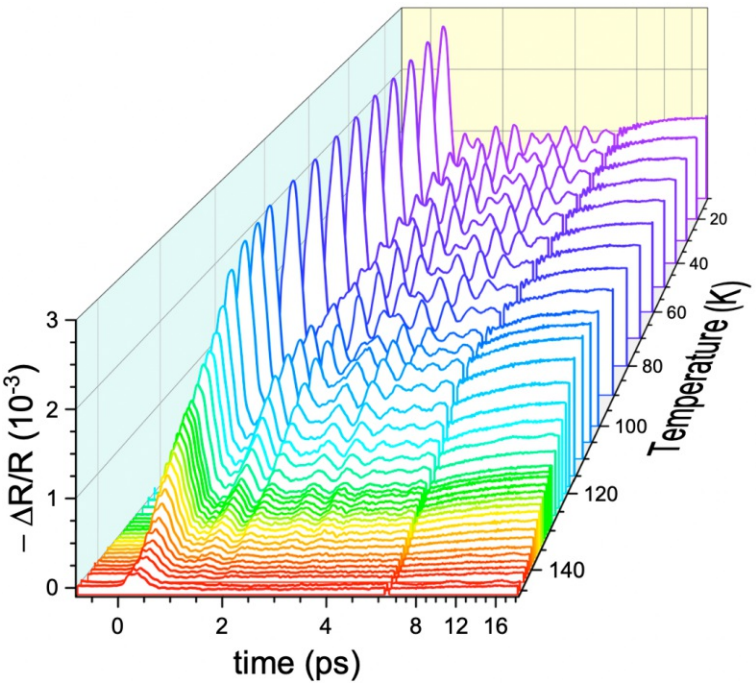

Figure 5.10: In-plane reflectivity traces of $BaNi_2As_2$ crystal between 10 and 146 K, measured upon heating. The measurements performed at constant fluence F = 0.4 mJ/cm^2 [69].

To analyse the T-dependence of the oscillatory and the overdamped components, the signal has to be decomposed as shown in Figure 5.11 for the data collected at 10 K. The overdamped components can be fitted by formula [55]

$$\frac{\Delta R}{R} = H(\sigma, t)\left[A_1 e^{-t/\tau_1} + B + A_2\left(1 - e^{-t/\tau_2}\right)\right] \qquad (5.12)$$

where $H(\sigma, t)$ presents the Heaviside step function with an effective rise time σ. The terms in brackets represent two processes. First is the fast-decaying process (of the order 1ps) with amplitude A_1, rise time τ_1 and the modulation offset B, while the second process is taking place on a 10-picosecond timescale with an amplitude A_2 and rise time τ_2, as shown on Fig. 5.11 [69].

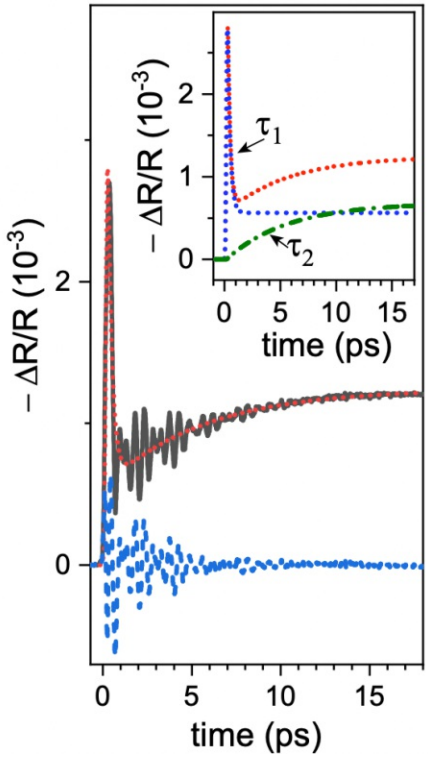

Figure 5.11: Decomposition of the reflectivity ⊿R/R at 10 K into overdamped (grey) and oscillatory (blue) components. Inset shows the individual overdamped components (blue and green line) together with the sum of both (red line) [69].

Fig. 5.12(a) and Fig. 5.12(b) shows the T-dependence of the Fast Fourier Transformation (FFT) of the residual signal after subtracting the best fits with Eq. (5.12) from the original transient reflectivity. The corresponding FFT spectra of the 10 K residual signal (blue curve in Fig. 5.11) is shown by the black line in Fig. 5.12(a). Several modes are clearly resolved at low temperatures, but all of them are vanishing above 146 K. Especially interesting are the modes, seen in the peaks of transient FFT at 1.57 and 2.05 THz [69]. The high frequency modes around 6 THz are weak and stronger damped, as observed from their reduced amplitude

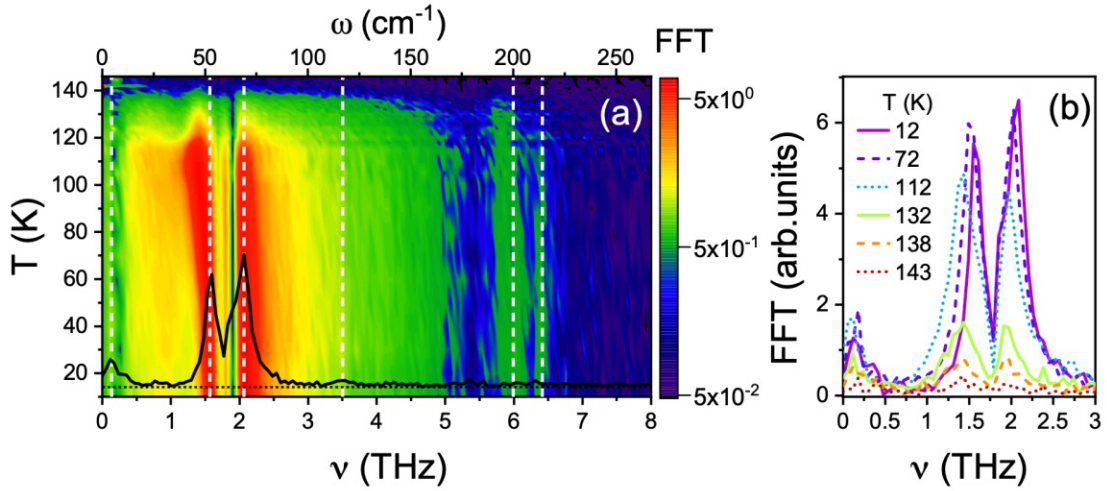

Figure 5.12: (a) The temperature dependence of FFT, demonstrating the presence of several modes at low temperatures (denoted by vertical dotted white lines). (b) Frequency dependent FFT spectra at selected temperatures [69].

Figure 5.13(a) presents the T- dependence of amplitudes A_1, A_2, and B, fitted with the Eq. (5.12). In CDW systems, the fast decay process (A_1,τ_1) has been attributed to an overdamped collective response of the CDW condensate [48, 61], while the slower process (A_2,τ_2) seems to be responsible for incoherently excited collective modes [61]. As both are related to the CDW order, their amplitudes should reflect these two processes. Here, structural phase transition temperature T_S and lock-in transition temperature T_l are denoted by the vertical dashed and dotted lines. The evolution of timescales τ_1 and τ_2 is shown in Figure 5.13(b).

In the commensurate CDW phase up to 110 K, the two timescales show similar dependence as in the prototype quasi-1D CDWs [48, 61], with τ_1 increasing while τ_2 decreasing with temperature [48, 61]. As τ_1 was shown to be inversely proportional to the CDW strength [48, 61], its T dependence is consistent with the observed softening of the oscillatory modes. Near T_1, τ_1 is reduced and remains nearly constant up to 146 K, similarly to frequencies and linewidths of the oscillatory modes. On the other hand, τ_2 displays an increase for $T \geq T_1$, although with the increasing temperature signals start to faint [69].

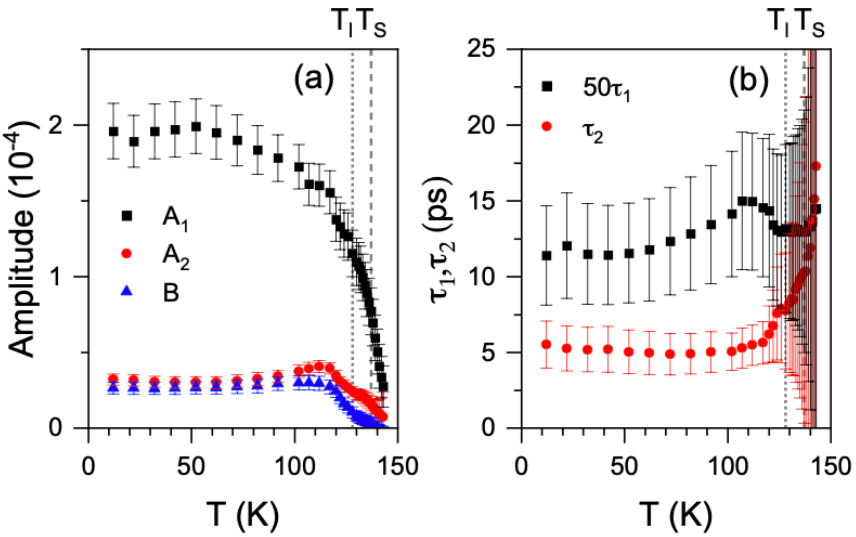

Figure 5.13: Temperature dependence of amplitudes (a) and relaxation times (b) of the electronic response, obtained by fitting the reflectivity transients using Eq. 5.12 [69].

Finally, fluence dependent study at constant temperature of 10 K was performed. Figure 5.14(a) shows no significant saturation of the overdamped response up to the highest fluence. Notably, saturation is commonly observed in fully gaped CDW systems, even at lower fluence. Such a saturation is commonly attributed to the photoinduced collapse of the CDW gap if the excess electronic energy exceeds the condensation energy [50]. Therefore, the absence of such a saturation in $BaNi_2As_2$ suggests that photoexcited carriers can effectively transfer their energy to the lattice just as in the high-temperature metallic phase [27] and thus imply absence of the CDW induced gap [13].

Nevertheless, the fact that amplitude signals show a strong *T*-dependence, provides strong evidence for the existence of the coupled electronic order. Especially the fluence dependence of $\tau_1(F)$ implies a continuous suppression of the underlying electronic order with increasing fluence, providing further support to the connection of the fast-decaying component with an overdamped mode, which in turn describes the recovery of the electronic part [48, 61]. Furthermore, the relaxation timescale τ_1 and the collective modes, are affected by the increasing excitation density, such as in the prototype CDW systems [50]. Moreover, the data in Fig. 5.14(a) clearly shows the sub-linear fluence dependence of the oscillatory modes. The most prominent are the strong fluence dependency of τ_1 and softening of the 1.57 THz modes, shown in panels (b) and (c) of Fig. 5.4, respectively. Both display similar behaviour to that observed in archetypical CDW system $K_{0.3}MoO_3$ [50].

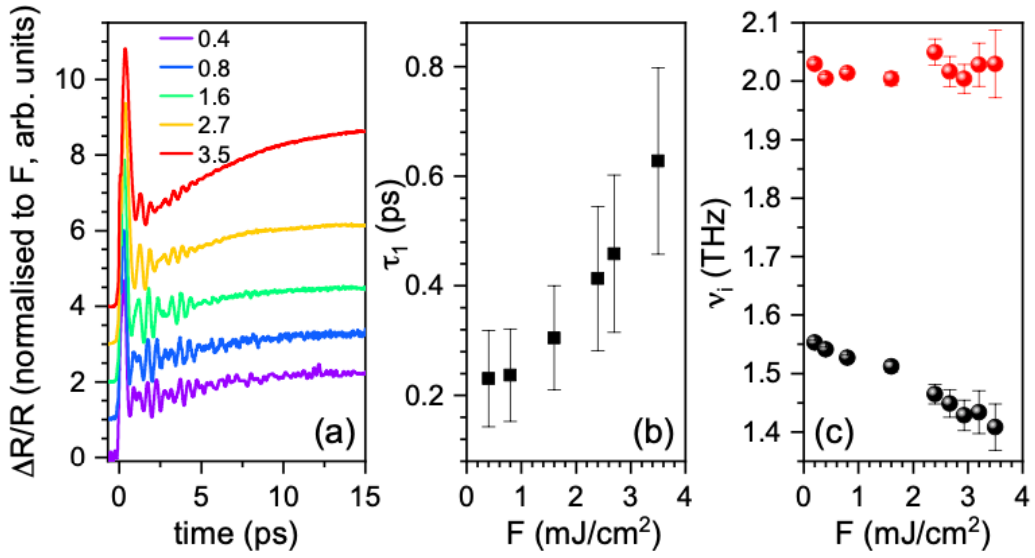

Figure 5.14: (a)Reflectivity transients normalized to excitation fluence in mJ/cm^2 at 10 K. (b) The extracted relaxation timescale τ_1 vs F at 10 K. F = 1 mJ/cm^2 corresponds to the absorbed energy density of about 50 J/cm^3. (c) Excitation density dependence of the frequencies of 1.57 THz (black) and 2.05 THz (red) modes at 10K [69].

The results presented above clearly demonstrate the existence of CDW collective modes in $BaNi_2As_2$. The extracted T-dependences of the amplitudes (A_1, A_2) and relaxation rates (τ_1,τ_2) provide further insights to the relation of CDWs and the structural phase transition. While the XRD data [9, 46] show two distinct modulations in the tetragonal and triclinic phases, the collective modes show no discontinuities at T_S. This suggests that commensurate CDW evolves from the incommensurate CDW by gaining additional periodicity along the c-axis. The sequence of phase transitions suggests a CDW driven nematicity in $BaNi_2As_2$ which may also be linked to the structural phase transition. The temperature and fluence dependence of the overdamped response imply the non-existence of an associated charge gap. As far as the microscopic origin of the charge instability driving the CDW order in $BaNi_2As_2$ is concerned, recent photoemission data [33] suggest the band reconstruction to be consistent with the proposed orbital selective Peierls instability [51]. Such a scenario is also supported by the finding of Ni-Ni dimers [46].

Chapter 6

6. Conclusion

The aim of this thesis was to identify of the signature of collective CDW amplitude modes and understand their evolution as a function of temperature (across the structural phase transition) and fluence in a $BaNi_2As_2$ metallic crystal.

First, Laue diffraction method was used to characterize and determine the orientation of the $BaNi_2As_2$ crystal in order to further measure the planar resistance. Material properties of $BaNi_2As_2$ were investigated with resistivity measurements at low temperatures and magnetic field, to characterize the sample quality by examining the CDW phase transitions. Indeed, the transition temperature of our samples is around ≈137 K, which corresponds to the transition temperatures reported in the literature. Moreover, the transition of our samples is sharp indicating that our samples are high-quality single crystals.

Time-resolved femtosecond optical spectroscopy was a prime experimental method of our choice, which enabled us to study formation of the CDW by following the response of a system on a perturbation in a controlled environment. The parameters we varied during measurements were the sample temperature and the excitation fluence of the laser beam in our optical pump-probe spectroscopy set-up. From the measured reflectivity as a function of both parameters, we were able to extract temperature dependences of the amplitudes of two collective modes (A_1, A_2) and their relaxation rates (τ_1,τ_2). From there we have concluded that the fast decay process (A_1,τ_1) can be attributed to an overdamped collective response of the CDW condensate, while the slower process (A_2,τ_2) is responsible for incoherently excited collective modes. Since, from the temperature dependence of the measured reflectivity, they are both related to the CDW order, we have clearly demonstrated the existence of CDW collective modes and revealed that they continuously evolve from commensurate to incommensurate CDW states across the phase transition. It is important to mention that all the conclusions in this thesis are in good agreement with previous studies of this material.

Many phenomena taking place in $BaNi_2As_2$ crystalline material remain to be uncovered or investigated in greater details. Among those is a possible competing between CDW order with superconductivity. In this view, future studies on systematic doping and pressure dependency of different physical observables (e.g., transport or pulse-probe induced change in reflectivity) may provide valuable additional clues to the underlying microscopic interactions.

Literature

[1] R. E. Peierls, Quantum Theory of Solids, Oxford University Press, 1. February 2001, London, ISBN: 9780198507819, DOI:10.1093/acprof:oso/9780198507819.001.0001

[2] H. Fröhlich, *On the Theory of Superconductivity: The One-Dimensional Case,* Proceedings of the Royal Society A: Mathematical, Physical and Engineering Sciences, 1954, Vol. 223, no.1154, p. 296–305, doi:10.1098/rspa.1954.0116

[3] W. Kohn, *Image of the Fermi Surface in the Vibration Spectrum of a Metal,* Physical Review Letters, 6 April 1959, Vol. 2, no. 9, p. 393–394, doi:10.1103/physrevlett.2.393

[4] J.G. Bednorz and K.A. Müller, *Possible High Tc Superconductivity in Ba-La-Cu-O System,* Zeitschrift für Physik B Condensed Matter, 1986, Vol. 64, p. 189-193, DOI: 10.1007/BF01303701

[5] B. Sipos, A. F. Kusmartseva, A. Akrap, H. Berger, L. Forrö and E. Tutis, *From Mott state to superconductivity in 1T-TaS_2,* Nature Materials, 7 December 2008, Vol. 7, p. 960–965, doi:10.1038/nmat2318

[6] M.Imada,A.Fujimori, & Y.Tokura, *Metal-insulator transitions,* Reviews of Modern Physics, 1998, Vol. 70, no. 4, p. 1039–1263, doi:10.1103/revmodphys.70.1039

[7] Maximilian Eichberger, Hanjo Schäfer, Marina Krumova, Markus Beyer, Jure Demsar, Helmuth Berger, Gustavo Moriena, German Sciaini, R. J. Dwayne Miller, *Snapshots of cooperative atomic motions in the optical suppression of charge density waves*, Nature Letters, 9. December 2010, Vol. 468, p. 799 – 802, DOI: 10.1038/nature09539

[8] Alaska Subedi, David J. Singh, *Density functional study of BaNi2As2,* Physical Review B 78, 27 October 2008, DOI: 10.1103/PhysRevB.78.132511

[9] Sangjun Lee, Gilberto A. de la Pena, Stella X.-L. Sun, Yizhi Fang, Matteo Mitrano, Hoyoung Jang, Jun-Sik Lee, Chris Eckberg, Daniel Campbell, John Collini Johnpierre Paglione F. M. F. de Groot and Peter Abbamonte, *Unconventional Charge Density Wave Order in the Pnictide Superconductor Ba(Ni1−xCox)2As2*, Phys. Rev. Lett., 12 April 2019, Vol. 122, no. 14, p. 147601, doi:10.1103/physrevlett.122.147601

[10] Z. G. Chen, G. Xu, W. Z. Hu, X. D. Zhang, P. Zheng, G. F. Chen, J. L. Luo, Z. Fang, and N. L. Wang, *Origin of the structural phase transition in BaNi2As2 at 130 K: A combined study of optical spectroscopy and band structure calculations,* Physical Review B 80, 8. September 2009, DOI: 10.1103/PhysRevB.80.094506

[11] Chelsey Dorow, *An Introduction to the Technique and Applications of Pump-Probe Spectroscopy*, Special Topic Paper, Physics 211A

[12] Zheng Li, Gengfu Chen, Jing Dong, Gang Li, Wanzheng Hu, Dan Wu, Shaokui Su,1 Ping Zheng, Tao Xiang, Nanlin Wang and Jianlin Luo, *Strong-coupling superconductivity in the nickel-based oxypnictide LaNiAsO1−xFx,* Physical Review B 78, 18 August 2008, DOI: 10.1103/PhysRevB.78.060504

[13] Z. G. Chen, W. Z. Hu, and N. L. Wang, *Different nature of instabilities in BaFe2As2 and BaNi2As2 as revealed by optical spectroscopy,* Phys. Status Solidi B 247, No. 3, 495–499, 8 February 2010, DOI: 10.1002/pssb.200983069

[14] Chris Eckberg, Limin Wang, Halyna Hodovanets, Hyunsoo Kim, Daniel J. Campbell, Peter Zavalij, Philip Piccoli, and Johnpierre Paglione, *Evolution of structure and superconductivity in Ba(Ni1−xCox)2As2*, Physical Review B 97, 7 June 2018, DOI: 10.1103/PhysRevB.97.224505

[15] F Ronning, N Kurita, E D Bauer, B L Scott, T Park, T Klimczuk, R Movshovich and J D Thompson, *The first order phase transition and superconductivity in BaNi2As2 single crystals,* J. Phys.: Condens. Matter 20, 6 August 2008, doi:10.1088/0953-8984/20/34/342203

[16] K. Kudo, M. Takasuga, Y. Okamoto, Z. Hiroi, and M. Nohara, *Giant Phonon Softening and Enhancement of Superconductivity by Phosphorus Doping of $BaNi_2As_2$,* Phys. Rev. Lett., 31 August 2012, no. 109, p. 097002, DOI: 10.1103/PhysRevLett.109.097002

[17] Eckberg, C., Campbell, D. J., Metz, T., Collini, J., Hodovanets, H., Drye, T., Paglione, J., *Sixfold enhancement of superconductivity in a tunable electronic nematic system,* Nature Physics, 23 December 2019, Vol. 16, p. 346, doi:10.1038/s41567-019-0736-9

[18] Masatsugu Sei Suzuki and Itsuko S. Suzuki, *Lecture Note on Charge density wave,* p. 2-4, Department of Physics, SUNY at Binghamton, 13. January 2012

[19] George Grüner, *The dynamics of charge-density waves*, Reviews of Modern Physics, Vol. 60, p. 1129-1148, 4. October 1988

[20] H.K.D.H. Bhadeshia, *Physical Metallurgy, Chapter 9.8, Phase changes and CDW*, Elsevier, 2015, ISBN 978-0-444-53770-6, DOI: 10.1016/C2010-0-65716-6

[21] Pierre Monceau, *Electronic crystals: an experimental overview*, Advances in Physics, Vol. 61, No. 4, p. 325-581, July-August 2012, ISSN: 1460-6976, DOI: 10.1080/00018732.2012.719674

[22] George Grüner, *Density waves in solids*, Frontiers in physics; v. 89. Addison-Wesly Pub- lishing Company, USA, 1994, ISBN: 0-201-62654-3

[23] K. Rossnagel, *On the origin of charge-density waves in select layered transition-metal dichalcogenides*, Journal of Physics: Condensed Matter, Vol. 23, No. 21, 11. May 2011, DOI: 10.1088/0953-8984/23/21/213001

[24] Xuetao Zhu, Yanwei Cao, Jiandi Zhang, E. W. Plummer, and Jiandong Guo, *Classification of charge density waves based on their nature*, PNAS, 24. Febraury 2015, Vol. 112, No. 8, p. 2367–2371, DOI: 10.1073/pnas.1424791112

[25] Xuetao Zhu, Jiandong Guo, Jiandi Zhang & E. W. Plummer, *Misconceptions associated with the origin of charge density waves,* Advances in Physics: X, 2017, Vol. 2, No. 3, p. 622-640, DOI: 10.1080/23746149.2017.1343098

[26] Sangjun Lee, Gilberto A. de la Pena, Stella X.-L. Sun, Yizhi Fang, Matteo Mitrano, Hoyoung Jang, Jun-Sik Lee, Chris Eckberg, Daniel Campbell, John Collini Johnpierre Paglione F. M. F. de Groot and Peter Abbamonte, *Discovery of a charge density wave instability in Co-doped BaNi2As2*, arXiv:1801.04874v1, 16 January 2018

[27] Obergfell, M., Demsar, J., *Tracking the Time Evolution of the Electron Distribution Function in Copper by Femtosecond Broadband Optical Spectroscopy,* Physical Review Letters, 21 January 2020, Vol. 124, no. 3, p. 037401, doi:10.1103/physrevlett.124.037401

[28] E.J. Woll and W. Kohn, *Images of the Fermi Surface in Phonon Spectra of Metals,* Physical Review, 1962, Vol.126, no. 5, p. 1693–1697, doi:10.1103/physrev.126.1693

[29] C. D. Malliakas, & M. G. Kanatzidis, *Charge Density Waves in the Square Nets of Tellurium of AMRETe4 (A= K, Na;M= Cu, Ag;RE= La, Ce),* Journal of the American Chemical Society, 14 August 2007, Vol. 129, no. 35, p. 10675–10677, DOI: 10.1021/ja073986m

[30] W. McMillan, *Theory of discommensurations and the commensurate-incommensurate charge-density-wave phase transition*, Phys. Rev. B, 1976, Vol. 14, p. 1496–1502, DOI:10.1103/PHYSREVB.14.1496

[31] J.Dumas and C.Schlenker, *Charge density wave properties of Molybdenum bronzes*, Int. J. Mod. Phys. B, 1993, Vol. 7, p. 4045-4108, DOI:10.1142/s0217979293003589

[32] H Ando, T Yokoya, K Ishizaka, S Tsuda, T Kiss, S Shin, T Eguchi, M Nohara and H Takagi, *Angle-resolved photoemission study of $K_{0.3}MoO_3$: direct observation of temperature-dependent Fermi surface across the Peierls transition*, Journal of Physics: Condensed matter, 29 July 2005, Vol.17, nr. 32, p. 4935 – 4940, DOI:10.1088/0953-8984/17/32/007

[33] Noda, T., Kudo, K., Takasuga, M., Nohara, M., Sugimoto, T., Ootsuki, D., Mizokawa, T., *Orbital-Dependent Band Renormalization in BaNi2(As1−xPx)2 (x = 0.00 and 0.092),* Journal of the Physical Society of Japan, 31 May 2017, Vol. 86, no. 8, p. 064708, doi:10.7566/jpsj.86.064708

[34] M. D. Johannes and I. I. Mazin, *Fermi surface nesting and the origin of charge density waves in metals,* Physical Review B, 30 April 2008, Vol. 77, p. 165135, DOI: 10.1103/PhysRevB.77.165135

[35] Soumyanarayanan, A., M. M. Yee, Y. He, J. van Wezel, D. J. Rahn, K. Rossnagel, E. W. Hudson, M. R. Norman, and J. E. Hoffman, *Quantum Phase Transition from Triangular to Stripe Charge Order in NbSe2*, Proceedings of the National Academy of Sciences, 29 January 2013, Vol. 110, no. 5, p. 1623–1627, doi:10.1073/pnas.1211387110

[36] Z. Z. Wang, J. C. Girard, C. Pasquier, D. Jerome, and K. Bechgaard, *Scanning tunneling microscopy in TTF-TCNQ: Phase and amplitude modulated charge density waves*, PHYSICAL REVIEW B, 5 March 2003, Vol. 67, p. 121401, DOI: 10.1103/PhysRevB.67.121401

[37] Kenji Koizumi, Kyoko Ishizaka, Takayuki Kiss, Mario Okawa, Reizo Kato, and Shik Shin, *Bulk-Sensitive Angle-Resolved Photoemission Spectroscopy on TTF-TCNQ*, Journal of the Physical Society of Japan, 28 January 2013, Vol.82, p. 025004, DOI: 10.7566/JPSJ.82.025004

[38] C.H. Chen, *Electron diffraction study of the charge-density wave superlattice in 2h-$nbse_2$,* Solid State Communications, Vol. 49, No. 7, p. 645-647, 1984, doi:10.1016/0038-1098(84)90211-4

[39] Du, C.-H., Lin, W. J., Su, Y., Tanner, B. K., Hatton, P. D., Casa, D., Hohl, H., *X-ray scattering studies of 2H-NbSe2, a superconductor and charge density wave material, under high external magnetic fields,* Journal of Physics: Condensed Matter, 14 April 2000, Vol. 12, nr. 25, p. 5361–5370, doi:10.1088/0953-8984/12/25/302

[40] Moncton, D. E., Axe, J. D., & DiSalvo, F. J., *Study of Superlattice Formation in 2H-NbSe2 and 2H-TaSe2 by Neutron Scattering,* Physical Review Letters, 24 March 1975, Vol. 34, nr. 12, p. 734–737, doi:10.1103/physrevlett.34.734

[41] Mook, H. A., & Watson, C. R., *Neutron Inelastic Scattering Study of Tetrathiafulvalene Tetracyanoquinodimethane (TTF-TCNQ),* Physical Review Letters, 5 April 1976, Vol. 36, no. 14, p. 801–803, doi:10.1103/physrevlett.36.801

[42] DiMasi, E., Aronson, M. C., Mansfield, J. F., Foran, B., & Lee, S., *Chemical pressure and charge-density waves in rare-earth tritelluride*S, Physical Review B, 15 November 1995, Vol. 52, no. 20, p. 14516–14525, doi:10.1103/physrevb.52.14516

[43] C. J. Arguello, S. P. Chockalingam, E. P. Rosenthal, L. Zhao, C. Gutie´rrez, J. H. Kang, W. C. Chung, *Visualizing the charge density wave transition in 2H-NbSe2 in real space,* PHYSICAL REVIEW B, Vol. 89, p.235115, 11 June 2014, DOI: 10.1103/PhysRevB.89.235115

[44] S. V. Borisenko, A. A. Kordyuk, A. N. Yaresko, V. B. Zabolotnyy, D. S. Inosov, R. Schuster, *Pseudogap and Charge Density Waves in Two Dimensions*, PRL, Vol. 100, p. 196402, 16 May 2008, DOI: 10.1103/PhysRevLett.100.196402

[45] P. M. Chaikin and T. C. Lubensky, *Principles of Condensed Matter Physics,* Cambridge University Press, 2000, ISBN: 0521794501

[46] Michael Merz, Liran Wang, Thomas Wolf, Peter Nagel, Christoph Meingast, and Stefan Schuppler, *Microscopic origin of the competition between charge density waves and enhanced superconductivity in Ba(Ni,Co)2(As,P)2,* arXiv:2012.05024, 9 December 2020

[47] Kusar, P., Kabanov, V. V., Demsar, J., Mertelj, T., Sugai, S., & Mihailovic, D., *Controlled Vaporization of the Superconducting Condensate in Cuprate Superconductors by Femtosecond Photoexcitation,* Physical Review Letters, 28 Nov. 2008, Vol. 101, nr. 22, DOI: 10.1103/physrevlett.101.227001

[48] H. Schäfer, V. V. Kabanov, M. Beyer, K. Biljakovic and J. Demsar, *Disentanglement of the Electronic and Lattice Parts of the Order Parameter in a 1D Charge Density Wave System Probed by Femtosecond Spectroscopy*, Physical review letters, 6 August 2010, Vol. 105, p. 066402, DOI: 10.1103/PhysRevLett.105.066402

[49] Dominko, D., Starešinić, D., Salamon, K., Biljaković, K., Tomeljak, A., Schäfer, H., Marcus, J., *Detection of charge density wave ground state in granular thin films of blue bronze K0.3MoO3by femtosecond spectroscopy,* Journal of Applied Physics, 12 July 2012, Vol. 110, nr. 1, p. 014907.doi:10.1063/1.3606418

[50] Tomeljak, A., Schäfer, H., Städter, D., Beyer, M., Biljakovic, K., & Demsar, J., *Dynamics of Photoinduced Charge-Density-Wave to Metal Phase Transition in K0.3MoO3*, Physical Review Letters, 13 Feburary 2009, Vol. 102, nr. 6, p. 066404
doi:10.1103/physrevlett.102.066404

[51] S.V. Streltsov & D.I. Khomskii, *Orbital-dependent singlet dimers and orbital-selective Peierls transitions in transition-metal compounds,* Physical Review B, 21 April 2014, Vol. 89, no. 16, doi:10.1103/physrevb.89.161112

[52] Paolo Foggi, Laura Bussotti, and Frederik V. R. Neuwahl, *Photophysical and photochemical applications of femtosecond time-resolved transient absorption spectroscopy,* International Journal of Photoenergy, Vol. 3, no. 2, p. 103-109, 2001, DOI: 10.1155/S1110662X01000125

[53] Andreas Othonos, *Probing ultrafast carrier and phonon dynamics in semiconductors,* J. Appl. Phys. 83, 1998, DOI: 10.1063/1.367411

[54] Anne Myers Kelley, *Condensed-phase molecular spectroscopy and Photophysics,* John Wiley & Sons Publication, 2013, ISBN 9780470946701

[55] H.J. Zeiger, J.Vidal, T.K.Cheng, E.P.Ippen, G.Dresselhaus and M.S.Dresselhaus, *Theory for displacive excitation of coherent phonons*, Phys. Rev. B, Vol. 45, no. 2, p. 768, 1 January 1992, DOI: 10.1103/PhysRevB.45.768

[56] I.Miccoli et al, *The 100th anniversary of the four-point probe technique: the role of probe geometries in isotropic and anisotropic systems*, J. Phys.: Condens. Matter, 18 May 2015, Vol. 27, no. 22, p. 223201, doi:10.1088/0953-8984/27/22/223201

[57] S.B.Fleicher, B.Pevzner, D.J.Daugherty, H.J.Zeiger, G.Dresselhaus, M.S.Dresselhaus, E.P.Ippen, A.F.Hebard, *Coherent phonons in alkali metal-doped C60,* Applied Physics Letters, 12 September 1997, Vol. 71, no. 19,p. 2734–2736, doi:10.1063/1.120121

[58] Sugai, S., Murase, K., Uchida, S., & Tanaka, S., *Comparison of the soft modes in tantalum dichalcogenides*, Physica B+C, May 1981, Vol. 105, no. 1-3, p. 405–409, doi:10.1016/0378-4363(81)90284-9

[59] J. Demsar, K. Biljakovic, and D. Mihailovic, *Single particle and collective excitations in the one- dimensional charge density wave solid K0.3MoO3 probed in real time by femtosecond spectroscopy*, Physical Review Letters, Vol. 83, no. 4, p. 800-803, 26 July 1999, doi:10.1103/physrevlett.83.800

[60] John G. Webster, *Electrical Measurement, Signal Processing, and Displays*, Chapter 7, 1st edition, CRC Press, 15 July 2003, ISBN 9780849317330

[61] Schaefer, H., Kabanov, V. V., & Demsar, J., *Collective modes in quasi-one-dimensional charge-density wave systems probed by femtosecond time-resolved optical studies,* Physical Review B, 6 January 2014, Vol. 89, no. 4, p. 045106, doi:10.1103/physrevb.89.045106

[62] Edbert Jarvis Sie, *Coherent Light-Matter Interactions in Monolayer Transition-Metal Dichalcogenides*, Springer International Publishing AG, 2018, Chapter 2, p. 13-25, DOI: 10.1007/978-3-319-69554-9, eBook ISBN: 978-3-319-69554-9

[63] Kuzmenko, A. B., *Kramers–Kronig constrained variational analysis of optical spectra,* Review of Scientific Instruments, Vol. 76, no. 8, p. 083108, 2005, doi:10.1063/1.1979470

[64] Liang Wang, Bin Zhou, Chester Shu, Sailing He, *Distributed Temperature Sensing Using Stimulated-Brillouin-Scattering-Based Slow Light,* IEEE Photonics Journal, Vol. 5, No. 6, December 2013, DOI: 10.1109/JPHOT.2013.2287557

[65] Jin, Y.-S., Jeon, S.-G., Kim, G.-J., Kim, J.-I., & Shon, C.-H., *Fast scanning of a pulsed terahertz signal using an oscillating optical delay line,* Review of Scientific Instruments, 5 February 2007, Vol. 78, no. 2, p. 023101, doi:10.1063/1.2437764

[66] K. R. Symon, *Mechanics*, 3. edition, p. 51, Addison-Wesley Publishing Company, Inc., Reading, Massachusetts, 1960

[67] Ru, N., Condron, C. L., Margulis, G. Y., Shin, K. Y., Laverock, J., Dugdale, S. B., Fisher, I. R., *Effect of chemical pressure on the charge density wave transition in rare-earth tritellurides RTe3,* Physical Review B, 14 January 2008, Vol. 77, no. 3, p. 035114, doi:10.1103/physrevb.77.035114

[68] Charles Kittel, *Introduction to Solid State Physics*, John Wiley & Sons, 8th edition, 2005, ISBN: 0-471-41526-X

[69] Vladimir Grigorev, Arjan Mejas, Amrit Raj Pokharel, Tao Dong, Amir A. Haghighirad, Rolf Heid, Yi Yao, Michael Merz, Matthieu Le Tacon, Jure Demsar, *Collective modes in $BaNi_2As_2$ probed by time-resolved spectroscopy*, 19 February 2021, arXiv:2102.09926

[70] L. A. Falkovsky, *Optical properties of graphene,* Journal of Physics: Conference Series, Vol. 129, p. 012004, doi:10.1088/1742-6596/129/1/012004

[71] Rohit P. Prasankumar and Antoinette J. Taylor, *Optical Techniques for Characterizing Complex Matter,* 1st Edition, Francis & Taylor, New York, 31 January 2012, ISBN 9780429192913

[72] H. Schäfer, *Disentanglement of the electronic and lattice parts of the order parameter in a 1D Charge Density Wave system probed by femtosecond spectroscopy,* PhD Thesis, Universität Konstanz, 2010